A Versatile Multi-Scale Framework for Transient Simulations of Solid Oxide Cells and Stack Modules Integrated in DETCHEM

To cite this article: Oscar Furst and Olaf Deutschmann 2025 *J. Electrochem. Soc.* **172** 074508

View the article online for updates and enhancements.

A Versatile Multi-Scale Framework for Transient Simulations of Solid Oxide Cells and Stack Modules Integrated in DETCHEM

Oscar Furst[ID] and Olaf Deutschmann[z][ID]

Institute for Chemical Technology and Polymer Chemistry (ITCP), Karlsruhe Institute of Technology, 76131 Karlsruhe, Germany

This paper presents the comprehensive multi-scale modeling framework integrated in the DETCHEM detailed chemistry software package, designed for the transient simulation of solid oxide cells (SOC), including button cells, planar repeating units, and stack modules. The framework uses a hierarchical approach, enabling calibration with button cell experiments and subsequent application to larger systems. Key features of the model include transient 1D simulations for generating electrochemical impedance spectra (EIS), spatially resolved mass and charge transport models for microstructure optimization, 2D mass and heat transport for planar cell simulations and a 3D homogenized model for performance analysis of SOC stack modules. Additionally, the model incorporates a thermocatalytic chemistry module to simulate the decomposition of a variety of fuels and an internal manifold model to study flow maldistribution in SOC stacks. The framework's versatility is demonstrated through case studies, including the calibration and validation of a co-electrolysis cell model using experimental EIS and polarization curves, transient simulations of ammonia-fed repeating units, and the evaluation of flow maldistribution effects in a stack module.

Nomenclature

Greek

α	[-]	Volume fraction
ϵ	[-]	Emissivity
Γ_{surf}	$[mol/m^2]$	Density of active sites on a catalyst
λ	$[W/m/K]$	Thermal conductivity
λ_{TPB}^V	$[1/m^2]$	Volumetric triple phase boundary length
μ	$[Pa\,s]$	Dynamic viscosity
ν	[-]	Stoichiometric coefficient
$\dot{\omega}$	$[mol/m^3/s]$	Species production rate (gas-phase reactions)
ϕ	$[V]$	Electric potential
ψ	[-]	Number of adsorption sites occupied
ρ	$[kg/m^3]$	Density
σ	$[S/m]$	Conductivity
θ	[-]	Surface coverage
ζ	[-]	Pressure loss coefficient

Latin

A_{DPB}^V	$[1/m]$	Volumetric double phase boundary area
C	$[F]$	Capacitance
c	$[mol/m^3]$	Concentration
c_p	$[J/kg/K]$	Specific heat capacity
E	$[V]$	Electric potential difference
E_a	$[J/mol]$	Activation energy
F	$[s\,A/mol]$	Faraday constant
G	$[J/mol]$	Gibbs energy
Gz	[-]	Grashof number
h	$[J/kg]$	Specific enthalpy
h_{conv}	$[W/m^2/K]$	Convective heat transfer coefficient
i_e^V	$[A/m^3]$	Charge transfer rate
I	$[A]$	Current
i	$[A/m^2]$	Current density
J	$[mol/m^2/s]$	Molar flux
k	Variable	Reaction rate constant
Nu	[-]	Nusselt number
p	$[Pa]$	Pressure
Pr	[-]	Prandtl number
q	$[W/m^2]$	Heat flux
$\dot{Q}$	$[W]$	Heat flow rate

(Continued).

$\dot{q}^V$	$[W/m^3]$	Volumetric heat production rate
Q	$[m^3/s]$	Flow rate
R	$[J/mol/K]$	Gas constant
Ra	[-]	Rayleigh number
$\mathbf{R}_{CT}$	[-]	Set of charge transfer reactions
Re	[-]	Reynolds number
$\mathbf{R}_{surf}$	[-]	Set of surface reactions
$\dot{s}$	$[mol/m^3/s]$	Species production rate (surface reactions)
$\mathbf{S}_g$	[-]	Set of gas species
$\mathbf{S}_{surf}$	[-]	Set of surface species
T	$[K]$	Temperature
u	$[m/s]$	Velocity
W	$[kg/mol]$	Molecular weight
X	[-]	Mole fraction
x, y, z	$[m]$	Spacial coordinates
Y	[-]	Mass fraction
Z	$[\Omega/m^2]$	Area specific impedance

In a future with a strong market penetration of renewable energy, chemical energy carriers will provide stable long-term energy storage and transportability. Hydrogen is predicted to be a cornerstone of this future energy market because it can be used as-is for power generation, or as chemical feedstock to be further processed into commodities and high value energy carriers.[1]

Solid Oxide Cells (SOCs) shape up to be a key technology in this scenario, as they boast high efficiencies utilized as both fuel cells and electrolyzers, and can be manufactured using more abundant catalyst materials than low-temperature electrochemical devices.[2] The SOC technology is undergoing its scale-up phase, with large manufacturing plants under construction[3] and multiple megawatt-scale SOC modules under operation.[4,5]

As interest in SOCs continues to grow, the modeling of Solid Oxide Electrolysis Cells (SOECs) and Solid Oxide Fuel Cells (SOFCs) becomes increasingly pertinent. Modeling is crucial throughout the entire life cycle of the cells, enhancing the effectiveness of their manufacture and optimizing the efficiency of their applications. The methodologies for simulating SOCs are as diverse as their applications, each tailored to meet specific requirements.

In systems modeling, when a performance prediction of a SOC integrated in a larger system is required, simulation speed is often as important as accuracy. In such applications, fast 0D models, which
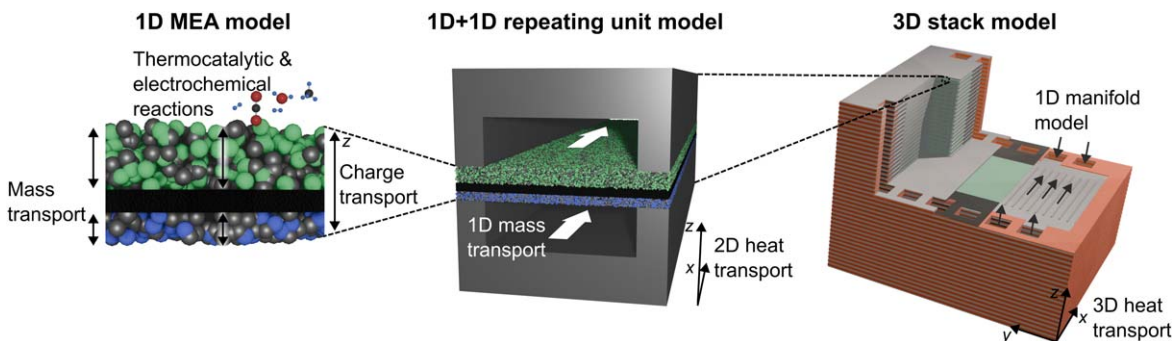
[z]E-mail: deutschmann@kit.edu

Figure 1. Illustration of the multi-scale modeling methodology. The 1D membrane electrode assembly (MEA) model is used for button cell simulations. It is complemented by a 1D channel model and 2D heat transport model to form a planar repeating unit (RU) model. The RU model can then be leveraged for 3D stack simulations.

are fitted to a specific cell design in a limited range of operating conditions using many experiments, are often the most appropriate ones.[6,7] These simple models serve the same purpose as surrogate models,[8,9] which circumvent modeling the physical phenomena altogether. Alternatively, some system models strike a balance between speed and accuracy by simulating a single cell representative for the performance of the whole stack.[10]

SOC models are also employed to optimize the design of the cells themselves, or the design of SOC stack modules.[11–13] In such cases, more detailed modeling approaches are warranted in order to ensure that all relevant physical processes are considered, especially when parameter variations are performed for which no experimental validation is available.[14] Such models also provide performance metrics inaccessible through experimentation alone, providing valuable information for the better design and operation of SOC.[15,16]

The most detailed simulation methodologies are used to enhance the understanding of the physical processes occurring within the cells. For example, simulating the electrochemical reaction using an elementary kinetic model may help to uncover the reaction pathways.[17,18] Modeling the chemical reactions responsible for the production of charge-carrying defects in ceramic conductors helps to understand the factors responsible for changes in the conductivity of ionic conductors.[19,20]

In this work, we present a flexible, multi-scale model designed for the transient simulation of button cells, planar repeating units and SOC stacks. The hierarchical approach, illustrated in Fig. 1, allows the calibration of the model to be performed with button cell experiments, which are the cheapest and fastest to perform, and to subsequently simulate repeating units and stacks.

The featured model, which is part of the DETCHEM[21] software package, includes the following capabilities:

• Transient 1D isothermal button cell simulations for the production of electrochemical impedance spectra (EIS) and polarization curves.
• Performance analysis of SOC modules through 2D repeating unit and 3D stack simulations considering transient heat transport.
• Microstructure optimization owing to the mass and charge transport models spacially resolved across the thickness of the membrane electrode assembly (MEA).
• A thermocatalytic chemistry model based on elementary reaction mechanisms compatible with a large database of mechanisms for the decomposition and production of hydrogen carriers.[22]
• Study of the influence of flow maldistribution in SOC stacks using an internal manifold model.

Compared to similar studies and previous versions of the software, the present modeling framework stands out with a fast and accurate internal manifold flow model, stack potential field computation algorithm and a conservative, transient 1D channel flow model.

A detailed exposition of the modeling framework is provided in the following Sections and concluded with a case-study of a Ni-YSZ/YSZ/LSM-YSZ cell for which experimental data were taken from literature in order to demonstrate the model's capability to predict SOC performance under various operating conditions, providing valuable insights for the design and optimization of SOC systems.

Methods

In the following sections, we present a comprehensive exposition of the DETCHEM^SOC model equations and solution algorithms. The first main Section pertains to the simulation of button cells and repeating units (1D MEA model and 1D+1D repeating unit model seen in Fig. 1), while the second main Section deals with the simulation of SOC stacks (3D stack model seen in Fig. 1).

This SOC model processes user-input parameters encompassing cell geometry, material properties, and physical characteristics to calculate the spatial distribution of species, temperatures, and current densities within the cells under the desired operating conditions.

Previous iterations of the modeling framework were described in our former studies[14,23–25] and a description of its current capabilities is provided herein. The parts of the modeling framework published before are briefly reiterated, while improvements and additions such as the improved channel flow model, stack potential field computation algorithm and the internal manifold model are given a more thorough description.

Planar solid oxide cell model.— *Mass and momentum transport.*—In order to be able to simulate transient phenomena in SOCs, such as the start-up, fluctuating inlet conditions and shut-down, a time-accurate model for the gas flow through the repeating unit gas channels and the button cell gas compartments was developed.

Bulk flow in planar repeating units: Since transient simulations are computationally intensive, computation times are kept reasonable through some simplifying assumptions which lead to a transient formulation of the plug flow model commonly used in chemical engineering. First, (i) a flow with a low Mach number is assumed. The low Mach number assumption is the broadest definition of incompressible flow, since its main implication is that pressure variations inside the flow are small enough to have a negligible impact on the density of the fluid, while still allowing changes in the fluid density through variations in temperature or composition.[26] Secondly, two of the main assumptions of the plug flow model are used, which are that (ii) diffusive mass transport along the channel is negligible compared to convective mass transport,[27] and that (iii) the flow can be assumed to be homogeneous across the channel cross-section due to its narrow geometry.[28]

An appropriate set of equations is obtained from the transport equations for low Mach number reacting laminar flows of Day and Bell[29] and removing diffusion terms:

$$\nabla{\cdot}\mathbf{u} = \frac{1}{\rho c_p T}\ \nabla{\cdot}\mathbf{q} + \frac{1}{\rho}\sum_{m \in \mathbf{S_g}}\left(\frac{W}{W_m} - \frac{h_m}{c_p T}\right)W_m\ \dot{\omega}_m \qquad [1]$$

$$\frac{\partial \rho\, Y_m}{\partial t} + \nabla{\cdot}\mathbf{u}\,\rho\, Y_m = W_m\ \dot{\omega}_m. \qquad [2]$$

with the velocity vector field $\mathbf{u}$, the heat flux vector field $\mathbf{q}$, molecular weight of the gas mixture W, specific enthalpy h_m, volume-specific production rate $\dot{\omega}_m$ and mass fraction Y_m of the species m which is part of the set of gas species $\mathbf{S_g}$.

These equations are then reduced to 1D (thereby satisfying the assumption of cross-section homogeneity) and discretized in space according to the finite volume method on a collocated grid using first order upwind interpolation of face values to yield a set of equations for the flow velocity, density and mass fractions. These equations are coupled to the heat transport equations presented later (Eq. 47) through the specific enthalpy h, the heat source term $\dot{Q}_{channel}$ (see Eq. 52) which appears as the surface integral of $\mathbf{q}$ and the enthalpy-dependent variables T and c_p.

The absence of momentum conservation equation is noteworthy. It is due to the assumption of 1D flow, resulting in a flow field that can be fully determined from Eq. 1. The momentum conservation equation becomes redundant unless the pressure gradient along the channel is of interest. Note that despite the low Mach number assumption, the pressure still varies throughout the flow due to viscous losses and variations in the density that are caused by changes in temperature and composition. However, the magnitude of these pressure changes are small enough to allow using a constant, homogeneous pressure field (commonly referred to as *thermodynamic pressure*) to evaluate the equation of state, while computing a variable, non-homogeneous pressure field (called the *mechanical pressure*) through the momentum equation and Eq. 1. This concept is sometimes referred to as *pressure filtering*.[28]

The boundary conditions at the inlet are straightforward, consisting of an inlet flux with specified velocity, temperature and mass fractions. Since the velocity profile across the channel cross-section is not resolved, entrance effects are not considered. Boundary conditions along the surface of the porous electrode, which, in the 1D model, manifest as source terms, need to be formulated carefully in order to yield a conservative set of equations. In the species conservation equation, the area-specific mass flux through the channel/electrode interface is expressed as $W_m\, J_m$, with the area-specific molar flux through the interface J_m computed according to the dusty gas model (DGM) (see Eq. 8). The bulk gas velocity across the electrode/channel interface, which results in a source term $u_{electrode}$ for the 1D discretization of Eq. 1, is computed as

$$u_{electrode} = \frac{RT}{p}\sum_{m \in \mathbf{S_g}} J_m. \qquad [3]$$

Thus, the final set of equations can be reformulated in 1D along the x axis with additional source terms:

$$\frac{\partial u}{\partial x} = \frac{1}{h_{channel}}u_{electrode}$$
$$+ \frac{1}{\rho c_p T}\frac{\partial}{\partial x}\left(\frac{\dot{Q}_{channel}}{h_{channel}\,w_{channel}}\right)$$
$$+ \frac{1}{\rho}\sum_{m \in \mathbf{S_g}}\left(\frac{W}{W_m} - \frac{h_m}{c_p T}\right)W_m\ \dot{\omega}_m \qquad [4]$$

$$\frac{\partial \rho\, Y_m}{\partial t} = -\frac{\partial u\, \rho\, Y_m}{\partial x} + W_m\ \dot{\omega}_m + \frac{1}{h_{channel}}W_m\, J_m \qquad [5]$$

with $h_{channel}$ and $w_{channel}$ the height and width of the channel.

Bulk flow in button cells: Since button cells are mainly used for the electrochemical characterization of cells, they are operated with a high mass flow rate of reactant in order to minimize the influence of mass transport in the gas compartments. Hence, the gas compartments can be assumed to be perfectly mixed and are simulated with a transient continuous stirred tank reactor model. Such a model was developed by Zhu and Kee and shown to accurately replicate the low frequency behavior of the system observed in EIS.[30] The aforementioned model uses a convective formulation of the mass conservation equation, which may lead to an accumulation of numerical errors in the density and mass fractions but perfect satisfaction of the equation of state. In order to conserve mass with a high accuracy throughout the computation, a transient CSTR model was developed by integrating the conservative Eqs. 1 and 2 over the volume of a gas compartment, assuming perfect mixing of the gas within and reformulating volume integral of divergence terms to surface integrals. The result is a set of equations very similar to the discretized formulation of Eqs. 1 and 2:

$$u_{in} + u_{electrode} - u_{out} = \frac{q_{channel}}{\rho c_p T} + \frac{h_{CSTR}}{\rho}$$
$$\times \sum_{m \in \mathbf{S_g}}\left(\frac{W}{W_m} - \frac{h_m}{c_p T}\right)W_m\ \dot{\omega}_m \qquad [6]$$

$$\frac{\partial \rho\, Y_m}{\partial t} + \frac{1}{h_{CSTR}}(u_{in}\rho_{in}Y_{m,in} - u_{out}\rho_{out}Y_{m,out}) = W_m\ \dot{\omega}_m \qquad [7]$$

with u_{in} and u_{out} the velocity of the incoming and outgoing flow respectively and h_{CSTR} the height of the gas compartment. $u_{electrode}$ is the velocity of the flow of gas from the porous electrode into the gas compartment, and $q_{channel}$ is the heat flux from the electrode into the gas compartment.

Due to the mostly homogeneous gas composition on both sides of the MEA, coplanar gradients inside the button cell are small. Therefore, the cell is assumed to be infinitely wide, leading to a purely 1D button cell model. Note that, in Eqs. 6 and 7, the infinitely wide surface facing the MEA is assumed to serve both as inlet and outlet in its entirety, since the subdivision of the surface in an inlet and outlet portion would only increase the inlet and outlet velocities by an arbitrary geometrical parameter without influencing the physical behavior of the gas compartment.

Compared to the model of Zhu and Kee,[30] this set of equations is conservative, but accumulates numerical errors in the equation of state (ideal gas law) as a trade-off.

Gas in the porous electrodes: Inside the MEA, mass transport in the normal direction is dominant. Consequently, it is assumed that gradients in coplanar directions can be neglected, allowing simulation of the mass trasport in the MEA through a 1D model. In the functional layer, diffusion layers and current-collecting layers of the porous electrodes, mass transport between the gas channel and the electrolyte is simulated in 1D using the dusty gas model (DGM). In the DGM, mass transport in a porous medium is assumed to be the result of three independent transport mechanisms: viscous flow driven by a pressure gradient, continuum diffusion and Knudsen diffusion.[31] In a 1D case, this results in the following expression for the area specific molar flux J_m of species $m \in \mathbf{S_g}$:[17,32]

$$J_m = -\left[\sum_{k \in \mathbf{S_g}} D_{mk}^{DGM}\frac{\partial c_k}{\partial z} + \left(\sum_{k \in \mathbf{S_g}}\frac{D_{mk}^{DGM}c_k}{D_{k,Kn}^{eff}}\right)\frac{B_g}{\mu}\frac{\partial p}{\partial z}\right] \qquad [8]$$

with

$$H_{ab} = \left[\frac{1}{D_{a,Kn}^{\text{eff}}} + \sum_{k \in \mathbf{S}_g \setminus a} \frac{X_k}{D_{ak}^{\text{eff}}} \right] \delta_{ab} + (\delta_{ab} - 1)\frac{X_a}{D_{ab}^{\text{eff}}} \quad [9]$$

$$D_{kl}^{\text{DGM}} = (\mathbf{H}^{-1})_{kl} \quad [10]$$

$$B_g = \frac{\alpha_{\text{pore}}^3 d_{\text{pore}}^2}{72 \, \tau_{\text{fac,pore}} (1 - \alpha_{\text{pore}})^2} \quad [11]$$

$$D_{k,Kn}^{\text{eff}} = \frac{\alpha_{\text{pore}}}{\tau_{\text{fac,pore}}} \frac{d_{\text{pore}}}{3} \sqrt{\frac{8RT}{\pi W_k}} \quad [12]$$

$$D_{kl}^{\text{eff}} = \frac{\alpha_{\text{pore}}}{\tau_{\text{fac,pore}}} D_{kl} \quad [13]$$

$$\tau_{\text{fac,pore}} = \left(1.23 \frac{(1 - \alpha_{\text{pore}})^{4/3}}{\alpha_{\text{pore}}} \right)^2. \quad [14]$$

where H_{ab} are the components of the matrix $\mathbf{H}$ for every combination of gas species a, $b \in [1, n(\mathbf{S}_g)]$, δ_{ab} is the Kronecker delta, α_{pore} is the porosity of the electrode, D_{kl} is the binary diffusion coefficient for gases k and l, μ is the dynamic viscosity of the gas mixture, p is the gas pressure, d_{pore} is the mean pore diameter, X_k is the mole fraction of species k in the gas mixture and c_k is its concentration.

A species conservation equation for the density $\rho_m = Y_m \rho$ of species $m \in \mathbf{S}_g$ in porous layers can subsequently be established, additionally considering source terms due to charge transfer reactions and thermocatalytic chemistry:[17,32]

$$\alpha_{\text{pore}} \frac{\partial Y_m \rho}{\partial t} = -\frac{\partial J_m W_m}{\partial z} + \sum_{r \in \mathbf{R}_{\text{CT}}} \frac{\nu_{m,r} i_{F,r}^V W_m}{n_{e,r} F} + W_m \dot{s}_m \quad [15]$$

where z is the spacial coordinate in MEA-normal direction, $\dot{s}_m$ is the production rate of species m through thermocatalytic reactions (see Eq. 18), $i_{F,r}^V$ is the Faradaic charge transfer rate in the chare transfer reaction $r \in \mathbf{R}_{\text{CT}}$ (see Eq. 22), $n_{e,r}$ is the number of electrons transferred in the charge transfer reaction and $\nu_{m,r}$ is the stoichiometric coefficient of species m in reaction r. The mass conservation equation for the total gas density ρ can be obtained as the sum of conservation equations for all species in $\mathbf{S}_g$. The pressure used in the computation of the flux J_m in Eq. 8 is computed using the ideal gas law.

At the channel/electrode boundary, the gas composition is assumed to be identical to the gas in the channel. The flux J_m computed at this interface using Eq. 8 couples the transport model of the porous layers to the bulk gas transport model. The electrode/electrolyte interface is assumed to be impermeable, the flux J_m therefore vanishing.

Thermocatalytic heterogeneous chemistry.—Depending on the type of fuel fed to the SOC, the heterogeneous chemistry on the catalytically active cell materials, typically nickel, needs to be considered. Common use-cases are direct ammonia fuel cells with internal ammonia cracking,[33,34] internal methane reforming in fuel cells fed with natural gas[17,35] and internal methanation during co-electrolysis of H_2O and CO_2.[36]

Considering surface chemistry in an electrode requires an additional set of variables, which are the surface coverage θ_m of the catalyst with the surface species $m \in \mathbf{S}_{\text{surf}}$. It is computed in a conservation equation as a function of the density of available active sites Γ_{surf} and the surface species production rate per catalyst surface area $\dot{s}_m^A$ as[24,28,37,38]

$$\frac{\partial \theta_m}{\partial t} = \frac{\psi_m \dot{s}_m^A}{\Gamma_{\text{surf}}} \quad [16]$$

where ψ_m is the number of adsorption sites covered by species $m \in \mathbf{S}_{\text{surf}}$.

The surface specific production rates $\dot{s}_m^A$ of gas-phase and surface species $m \in \mathbf{S}_g \cup \mathbf{S}_{\text{surf}}$, in turn, are computed from a set of elementary kinetic reactions $r \in \mathbf{R}_{\text{surf}}$ as follows:

$$\dot{s}_m^A = \sum_{r \in \mathbf{R}_{\text{surf}}} (\nu''_{m,r} - \nu'_{m,r}) \, k_{f,r} \prod_{k \in \mathbf{S}_g \cup \mathbf{S}_{\text{surf}}} c_k^{\nu'_{k,r}} \quad [17]$$

where $\nu'_{m,r}$ and $\nu''_{m,r}$ are the stoichiometric coefficients of species m as reactant and product in reaction r and $k_{f,r}$ is the forward reaction rate constant. c_k is the concentration of species k, which has a dimension of [mol m^{-3}] for a gas species and [mol m^{-2}] for a surface species. Accordingly, the dimension of $k_{f,r}$ varies with the dimensions of c_k and the stoichiometric coefficients $\nu''_{k,r}$. The production rates for surface species enter the source term of Eq. 16. The volumetric gas species m production rates $\dot{s}_m$ used in Eq. 15 is obtained by multiplying the surface specific production rate $\dot{s}_m^A$ with the catalyst surface area per unit volume, which is usually the surface area of the metallic phase:

$$\dot{s}_m = \dot{s}_m^A A_{\text{cat}}^V. \quad [18]$$

The reaction rate constants k_f are computed as:[38]

$$k_{f,r} = A_r T^{\kappa_r} \exp\left(-\frac{E_{a,r}}{RT}\right) \prod_{k \in \mathbf{S}_{\text{surf}}} \exp\left(-\frac{\xi_{k,r} \theta_k}{RT}\right). \quad [19]$$

where A is the pre-exponential factor, κ introduces a temperature dependence on the pre-exponential factor, E_a is the activation energy of the reaction and $\xi_{k,r}$ regulates the influence of surface coverages of species k on the activation energy of the reaction r in order to account for lateral interactions. These variables are unique to each reaction and are determined along with the reaction mechanism itself. In the case-study performed herein, a reaction mechanism of methane reforming and water-gas shift on nickel consisting of 42 elementary steps is used,[39] but other mechanisms may be used to model other fuel or electrode compositions.[22]

The thermodynamic consistency of these mechanism is guaranteed using the method outlined by Maier et al.[38] which ensures that the ratio of forward and backward reaction rate constants correspond to the thermodynamic equilibriums. Reactions are only paired as forward and backward reactions for the purpose of adjusting thermodynamic consistency. Otherwise, all reaction equations of a given mechanism are considered forward reactions for the purpose of Eqs. 17 and 19.

Electrochemical model.—In a fuel cell model, the electrochemical model is the central component which determines the relationship between the cell potential E_{cell} and the achieved current density i.

In DETCHEM$^{\text{SOC}}$, the electrochemical reaction rates are modeled using a modified Butler-Volmer equation, which links the local half-cell activation overpotential η_{act} to the resulting local charge transfer rate per unit length or area $i_r^{A/\lambda}$ of the charge transfer reaction r:

$$i_r^{A/\lambda} = i_{0,r} \left[\exp\left(\frac{\beta_a F n_{e,r} \eta_{\text{act}}}{RT}\right) - \exp\left(-\frac{\beta_c F n_{e,r} \eta_{\text{act}}}{RT}\right) \right] \quad [20]$$

where $i_{0,r}$ is the exchange current density and $n_{e,r}$ is the number of elementary charges transferred. β_a and β_c are the anodic and

cathodic charge transfer coefficients, which depend on the elementary reactions involved in the charge transfer mechanism.

The exact expressions used to compute the exchange current densities $i_{0,r}$ depend on the electrode materials,[17,40] but take the following general form:

$$i_{0,r} = A_r \exp\left(-\frac{E_r}{RT}\right) f(p_s) \qquad [21]$$

with a pre-factor A_r, an activation energy E_r and a function of the gas partial pressures $f(p_s)$. The exchange current density is expressed in A/cm in a cermet electrode and in A/cm² in a mixed ionic-electronic conductor electrode.

While the Butler-Volmer equation is derived from transition state theory strictly for single-step, single-electron transfer reactions, it remains an excellent approximation even for multistep reactions involving multiple electron transfers.[41] In such cases, the charge transfer coefficients and the exchange current densities are treated as fitting parameters adjusted to experimental data. Thus, it is used as an empirical correlation with only loose connection to the reaction mechanism. In modeling studies of reversible SOCs, the same kinetic rate equation is often successfully applied to pairs of oxidation and reduction equations, e.g., the oxygen evolution reaction and the oxygen reduction reaction.[42–44] While this may suggest similar electrocatalytic activity of the electrode for both reactions, such empirical modeling approaches are not suited for drawing precise conclusions about the underlying reaction mechanisms.

Table III shows the expressions used to compute the exchange current densities in the case-study performed herein. In this study, the LSM-YSZ air electrode and the Ni-YSZ fuel electrode are both cermet electrodes, which results in the reactions taking place over the triples phase boundary between the gas, the metallic phase and the ceramic phase λ_{TPB}^V. Therefore, the local Faradaic charge transfer rate $i_{F,r}^V$ for reaction r is obtained as follows:

$$i_{F,r}^V = i_r^\lambda \, \lambda_{TPB}^V \qquad [22]$$

The superscript V indicates volumetric quantities, i.e., triple phase boundary (TPB) length per unit volume.

The activation overpotential η_{act} is determined from the local potential of the electron- and ion-conducting phases ϕ_{el} and ϕ_{io} and the local reversible half-cell reaction potential $E_{rev,r}$ depending on the considered reaction r:[45]

$$E_{rev,H_2} = \frac{\Delta G_{H_2O}^{0,f} - \Delta G_{H_2}^{0,f}}{n_{e,r}F} + \frac{RT}{n_{e,r}F} \ln\left(\frac{p_{H_2O}}{p_{H_2}}\right) \qquad [23]$$

$$E_{rev,CO} = \frac{\Delta G_{CO_2}^{0,f} - \Delta G_{CO}^{0,f}}{n_{e,r}F} + \frac{RT}{n_{e,r}F} \ln\left(\frac{p_{CO_2}}{p_{CO}}\right) \qquad [24]$$

$$E_{rev,O_2} = \frac{\Delta G_{O_2}^{0,f}}{n_{e,r}F} + \frac{RT}{n_{e,r}F} \ln\left(\left(\frac{p_{O_2}}{p_{atm}}\right)^{0.5}\right) \qquad [25]$$

$$\eta_{act} = \phi_{el} - \phi_{io} - E_{rev} \qquad [26]$$

where $p_{atm} = 101325$ Pa and $\Delta G_m^{0,f}$ is the Gibbs free energy of formation of species m at temperature T.

In cases where the fuel composition allows both H_2 and CO reaction pathways, charge transfer rates i_{H_2/H_2O}^λ and i_{CO/CO_2}^λ are computed for both half-cell reactions. However, as the reaction sites are shared by both reaction pathways, the actual charge transfer rate in the fuel electrode is computed as the sum of both half cell reaction

charge transfer rates weighted by the mole fractions of H_2O and CO_2:[24]

$$i_{total}^\lambda = w \, i_{H_2/H_2O}^\lambda + (1 - w) \, i_{CO/CO_2}^\lambda \qquad [27]$$

with

$$w = \frac{X_{H_2O}}{X_{H_2O} + X_{CO_2}} \qquad [28]$$

where the mole fractions correspond to the local composition of the gas phase, which changes across the thickness of the electrode according to the mass transport model.

Charge transport.—Since the electrochemical model computes the charge transfer rate over the full height of both electrodes (as opposed to just the porous electrode/bulk electrolyte interface, which is often assumed in simplified models), the overpotential η needs to be known at every point of the electrode. The potential fields ϕ_{el} and ϕ_{io} (electron-conducting and ion-conducting phase), which in term depend on the current density fields i_{el} and i_{io}, therefore need to be computed using a charge transport model.

The present distributed charge transport model considers the movement of charged particles, usually electrons e' in the electron-conducting phases and oxygen vacancies $V_{\ddot{O}}$ in the ion-conducting phases, produced throughout the porous electrodes by charge transfer reactions. As is common in SOC literature, the terms *anode*, *cathode* and *electrode* are used herein to refer to all the solid phases of the porous structures on either sides of the impermeable bulk electrolyte, and *electrolyte* refers to the impermeable membrane.

In the present cell model, a simplified implementation of the distributed charge transfer model developed by Zhu et al.[46] is used, which is a Nernst-Planck equation simplified with the assumption that the charge transport due to species concentration gradients can be neglected. Therefore, the current density in the phase $m \in \{el, io\}$ is proportional to its effective conductivity σ_m^{eff} (see Eq. 45) and the local potential gradient:

$$i_m = \sigma_m^{eff} \frac{\partial \phi_m}{\partial z} \qquad [29]$$

The divergence of the electronic and ionic current density describes the amount of charge carriers produced in their respective phases, which is the charge transfer rate i_e^V. Under the assumption of electroneutrality, the accumulation of charge in both phases is equilibrated so that the charge transfer rates for the electronic and ionic phases are complementary:

$$\frac{\partial i_{el}}{\partial z} = i_e^V \qquad [30]$$

$$\frac{\partial i_{io}}{\partial z} = -i_e^V. \qquad [31]$$

Boundary conditions and the ability to evaluate the charge transfer rate i_e^V as a function of known variables close the system of equations and allows the computation of the potential fields ϕ_{el} and ϕ_{io}.

Herein, the charge transfer rate is assumed to be composed of the Faradaic charge transfer rate i_F^V and the double layer charge transfer rate i_{DL}^V:

$$i_e^V = i_F^V + i_{DL}^V \qquad [32]$$

The former is computed according to Eq. 22 while the latter is computed according to a plate capacitor model[18]

$$\frac{\partial}{\partial t}(\phi_{el} - \phi_{io}) = \frac{i_{DL}^V}{C_{DL} \cdot A_{el/io}^V} \qquad [33]$$

where C_{DL} is the double-layer capacitance of the phase boundary between the ion-conducting phase and the electron-conducting phase per double-layer surface area and $A_{el/io}^V$ is the phase boundary per unit volume.

The only transient component of the charge transport model is the charging of the double layer, which is relevant for the simulation of impedance spectra. Since double-layer charging has a very short time-scale, i_{DL}^V can be assumed to vanish for all other types of simulations. In such cases, the discretized form of Eqs. 30 and 31 are integrated with the secant method.

As boundary conditions for the electron-conducting phase, a reference potential of E_{cell} is set at the cathode/air channel boundary and a reference potential of 0 V is set at the anode/fuel channel boundary. If the bulk electrolyte is a pure ion conductor, the electron flux must also vanish at the cathode/electrolyte and anode/electrolyte boundaries. In the ion-conducting phase, which exists in the cathode, electrolyte and anode, the ion flux must vanish at the cathode/air channel and anode/fuel channel boundaries.

Contact resistances can also be considered at such interfaces. As contact resistance is difficult to measure or predict, in this study the contact resistances are assumed to be the difference between measured ohmic resistance of the SOC (measured through EIS) and computed resistance of the electrolyte (determined from its geometry and conductivity measurements from literature), concentrated at the fuel electrode/electrolyte boundary.

Microstructure model.—In order to simulate the gas transport in the electrodes using the dusty gas model, charge transport through the porous conductors and electrochemical kinetics at the double and triple phase boundaries, it is of paramount importance to know a number of morphological characteristics of the electrodes such as its porosity, tortuosity, pore diameters, phase boundary areas and triple phase boundary lengths.

While a number of such properties can be determined experimentally or through numerical simulation of the sintering process, it is generally more economical to approximate these properties using analytical expressions derived from percolation theory. Since the fabrication process has a great influence on the morphology of the electrode, the set of expressions used to evaluate most parameters differs between cermet electrodes and infiltrated electrodes.

To evaluate the properties of cermet electrodes, the percolation model developed by Bertei and Nicolella is used.[14,47,48] Assuming an electrode composed of three phases, comprising pores and two solid phases m and n, a central component of the model is the percolation probability γ_k of the phase $k \in \{n, m\}$, which is computed using the following empirical correlation:[14,47]

$$\gamma_k = 1 - \left(\frac{4.236 - Z_{k,k}}{2.472}\right)^{3.7} \qquad [34]$$

where $Z_{k,k}$ is the average contact number between k-particles.

The volume-specific length of the triple phase boundary λ_{TPB}^V can then be computed as:[14,48]

$$\lambda_{TPB}^V = 1.92\pi \left(\min(r_{p,m}, \ r_{p,n})\sin\frac{\pi}{12}\right) n_m^V \ Z_{m,n} \ \gamma_m \gamma_n \qquad [35]$$

where $r_{p,k}$ is the mean radius of particles of the solid phase $k \in \{n, m\}$, n_k^V is the volume-specific number of particles in the electrode after sintering and $Z_{m,n}$ is the average contact number between m-particles and n-particles. Therein, an initial porosity before sintering of 0.36 is assumed.[48]

n_m^V and $Z_{m,n}$ can, in turn, be evaluated from the particle diameters and phase volume fractions through a series of expressions derived by Bertei and Nicolella[48] and not repeated here for the sake of clarity.

The volume-specific area $A_{m/n}^V$ of the boundary between solid phases m and n can be computed in a similar fashion:[48]

$$A_{m/n}^V = 0.96\,\pi \left(\min(r_{p,m}, \ r_{p,n})\sin\frac{\pi}{12}\right)^2 n_m^V \ Z_{m,n} \ \gamma_m \gamma_n \qquad [36]$$

The volume-specific area of the boundary between phase $k \in \{n, m\}$ and the gas is computed as[45]

$$A_{k/gas}^V = 4\pi r_{p,k}^2 n_k^V \qquad [37]$$

and the mean pore diameter d_{pore} as[14]

$$d_{pore} = \frac{2}{3}\frac{\alpha_{pore}}{1 - \alpha_{pore,BS}}\frac{d_m d_n}{\alpha_{m,BS}d_n + \alpha_{n,BS}d_m} \qquad [38]$$

where d_k is the mean particle diameter of the phase $k \in \{n, m\}$ and $\alpha_{k,BS}$ is the volume fraction of the phase k before sintering.

To evaluate the properties of infiltrated electrodes, the percolation model developed by Vijay et al.[49] is used. By nature, the backbone of infiltrated electrodes is necessarily percolating, leaving only the percolation probabilities of the infiltrated nanoparticles n and the pores to be determined using the following empirical relations[14,49]

$$\gamma_n = \left(1 - \left(\frac{0.75 - S_n}{0.25}\right)^{0.52}\right)^{0.097} \qquad [39]$$

$$\gamma_{pore} = \left(1 - \left(\frac{0.2 - \alpha_{pore}}{0.15}\right)^{2.68}\right)^{0.25} \qquad [40]$$

where S_n is the surface area fraction of nanoparticles n computed as

$$S_n = \frac{\alpha_n \pi d_n^2}{\alpha_n \pi d_n^2 + \alpha_m \pi d_m^2}. \qquad [41]$$

The volume-specific length of the triple phase boundary λ_{TPB}^V is computed as:[14,49]

$$\lambda_{TPB}^V = 2\pi r_{p,n} n_n^V \ Z_{n,m} \ \gamma_n \gamma_{pore} \qquad [42]$$

in which phase n is the infiltrated nanoparticle phase while m is the backbone phase. In the case of infiltrated electrodes, the coordination number $Z_{n,m}$ can be computed from the lengthy but straightforward process detailed by Vijay et al.[49]

The volume-specific interfacial area $A_{m/n}^V$ is computed as

$$A_{m/n}^V = \pi r_{p,n}^2 n_n^V \ Z_{n,m} \ \gamma_n \qquad [43]$$

and the mean pore diameter d_{pore} as

$$d_{pore} = \frac{2}{3}\frac{\alpha_{pore}}{1 - \alpha_{pore}}d_m. \qquad [44]$$

In both infiltrated and cermet electrodes, the effective conductivity σ_k^{eff} of phase $k \in \{n, m\}$ is estimated from the conductivity of the dense material $\sigma_{mat,k}$:[14,50]

$$\sigma_k^{eff} = \sigma_{mat,k}[(1 - \alpha_{pore})\alpha_k \gamma_k]^{1.5}. \qquad [45]$$

The tortuosity of the pores, when it cannot be measured, is approximated using the following expression developed by Lanfrey

et al. for random packings of identical particles:[51]

$$\tau_{\text{pore}} = \left(1.23\,\frac{(1-\epsilon)^{4/3}}{\epsilon}\right)^2 \quad [46]$$

Heat transport.—While button cells can generally be assumed to be operated isothermally due to their small dimensions and the typically high gas flow rates, the performance of larger planar SOCs is significantly impacted by temperature gradients along the MEA. Therefore, a heat transport model that takes into account all significant heat sources and sinks is critical for the accuracy of planar SOC simulations.

Experimental data which can be used to validate such models are rare, but the present heat transport model has been validated in the past by Wehrle et al.[25]

Bulk gas in planar cells: Heat transport through the gas channels is computed using an energy conservation equation derived from the model of Day and Bell[29] in the same fashion as the mass transport model presented in Eqs. 4–5:

$$\frac{\partial \rho\, h}{\partial t} = -\nabla \cdot \mathbf{u}\, \rho\, h \quad [47]$$

where h is the specific enthalpy of the gas mixture. Therein, heat transfer between the gas and the neighboring solid phase manifests as a boundary condition. When the equations are discretized and reduced to a single dimension along the gas channel length, the heat transfer can be treated as a source term $\dot{Q}_{\text{channel}}$. This source term is evaluated from an empirical expression for the Nusselt number Nu in the fully developed laminar flow of catalytic monolith channels,[52] which allows the computation of the heat transfer coefficient h_{conv}:

$$h_{\text{conv}} = \frac{Nu\,\lambda_{\text{g}}}{d_{\text{h}}} \quad [48]$$

$$Nu = 3.095 + 8.933 \left(\frac{1000}{Gz}\right)^{-0.5386} \exp\left(-\frac{6.7275}{Gz}\right) \quad [49]$$

$$Gz = \frac{d_{\text{h}}}{x}\, Re\, Pr \quad [50]$$

$$d_{\text{h}} = \frac{2\, w_{\text{channel}}\, h_{\text{channel}}}{w_{\text{channel}} + h_{\text{channel}}} \quad [51]$$

where λ_g is the heat conductivity of the gas, d_{h} is the hydraulic diameter of the channel, x is the distance to the channel inlet, w_{channel} is the width of the channel, h_{channel} is the height of the channel, Re is the Reynolds number of the flow and Pr is the Prandtl number of the fluid.

The heat transfer coefficient h_{conv} allows to compute the heat flux through the lateral boundaries of the channels, which can be different on every side depending on the solid surface temperatures T_{solid}:

$$q_{\text{conv}} = h_{\text{conv}}\, (T_{\text{solid}} - T). \quad [52]$$

$\dot{Q}_{\text{channel}}$ is the surface integral of boundary fluxes q_{conv} over the gas/solid interface. Discretized with a first order method, the integral is simply the sum of all boundary fluxes q_{conv} at the four side of the channel multiplied by their corresponding surface areas.

Since the specific enthalpy h is a nonlinear function of the gas temperature T, the temperature is determined iteratively using the Newton method.

Solid phase: For the solid phase, the following 2D heat diffusion equation is solved:[24]

$$\rho^{\text{eff}} c_p^{\text{eff}} \frac{\partial T}{\partial t} = \nabla \cdot \lambda^{\text{eff}}\, \nabla T + \dot{q}_{\text{solid}}^{V} \quad [53]$$

The density ρ^{eff}, specific heat capacity c_p^{eff} and thermal conductivity λ^{eff} are expressed as effective homogenized properties of the considered layers (e.g., porous support layer, cermet electrode, bulk electrolyte), taking into account their porosities and compositions:

$$\rho_l^{\text{eff}} = \sum_{m \in \mathbf{M}_l} \alpha_{m,l}\rho_m \quad [54]$$

$$c_{p,l}^{\text{eff}} = \sum_{m \in \mathbf{M}_l} \alpha_{m,l}c_{p,m} \quad [55]$$

$$\lambda_l^{\text{eff}} = \sum_{m \in \mathbf{M}_l} \alpha_{m,l}\lambda_m \quad [56]$$

with $\alpha_{m,l}$ being the volume fraction of the material m from the set of solid materials $\mathbf{M}_l$ in the layer l.

In the heat diffusion equation, $\dot{q}_{\text{solid}}^{V}$ represents the sum heat source terms per unit volume, which differ depending on the location in the cell. In the fuel electrode, it includes endothermic or exothermic thermocatalytic reactions:

$$\dot{q}_{\text{schem}}^{V} = -\sum_{k \in \mathbf{S}_{\text{g}}} h_k \dot{s}_k W_k. \quad [57]$$

The reversible reaction heat $\dot{q}_{\text{echem}}^{V}$ from the charge transfer reactions

$$\dot{q}_{\text{echem}}^{V} = -\sum_{r \in \mathbf{R}_{\text{CT}}} \frac{i_{F,r}^{V}}{n_{e,r}\, F} T \Delta s_r \quad [58]$$

with the molar reaction entropy Δs_r is also assumed to be entirely released in the fuel electrode, since computing the reaction heat from half-cell reaction would require thermodynamic properties of charge carriers which are difficult to determine. In both electrodes, $\dot{q}_{\text{solid}}^{V}$ also includes activation losses $\dot{q}_{\text{act}}^{V}$ from the charge transfer reactions:

$$\dot{q}_{\text{act}}^{V} = \eta_{\text{act},r}\, i_{F,r}^{V} \quad [59]$$

Since all layers conduct charge carriers, $\dot{q}_{\text{solid}}^{V}$ also includes joule heating $\dot{q}_{\text{joule}}^{V}$, computes as

$$\dot{q}_{\text{joule}}^{V} = \frac{i_{\text{el}}^2}{\sigma_{\text{el}}^{\text{eff}}} + \frac{i_{\text{io}}^2}{\sigma_{\text{io}}^{\text{eff}}} \quad [60]$$

with the effective conductivities of the electron and ion conducting phases σ^{eff} and the current densities i. Additionally, contact resistances R_{cont} between all layers (current collectors, electrodes, barrier layers, electrolyte) are taken into account, which induce additional joule heating:

$$q_{\text{joule,cont}} = i^2 R_{\text{cont}}. \quad [61]$$

Joule heating through contact resistance is area specific, but is implemented as a volumetric heat source in the adjacent discretized volume of the neighboring electrode.

The surface of the electrode, where the electrode/channel interface is located, requires special consideration because it is simultaneously in contact with the ribs of the interconnect. Although the cell model is 2D, these ribs are still considered and can be imagined to form a porous layer connecting the electrode with the bulk of the interconnect. However, these layers are treated differently than the

porous electrode layers because the heat transfer mechanisms are different.

First, the diffusive heat transport term of Eq. 53 applies to the interface between electrode and ribs, only that it needs to be adjusted for the reduced contact area between the two. Then, due to the high temperatures in SOC, heat transport between interconnect and electrode through radiation at the channel surfaces also needs to be considered. It is modeled as the following heat flux:[24]

$$q_{\text{rad}} = \frac{\sigma_{\text{SB}}(T_{\text{ede}}^4 - T_{\text{ic}}^4)}{R_{\text{rad,ede}\to\text{ic}}} \quad [62]$$

with the electrode surface temperature T_{ede}, the interconnect surface temperature T_{ic} and the Stefan-Boltzmann constant σ_{SB}. Since the metallic interconnect typically has a much higher thermal conductivity than the MEA, and the interconnect is very long compared to its height, its temperature is assumed to be homogeneous across its height. Like Joule heating through contact resistances, the heat flux is implemented as volumetric source term applied to the concerned discretized volumes.

$R_{\text{rad,ede}\to\text{ic}}$ is the thermal resistance to radiation, and includes the dimensions of the channel w_{channel} and h_{channel}, the view factors F between these areas and their total emissivities ϵ:[24]

$$R_{\text{rad,ede}\to\text{ic}} = \frac{1 - \epsilon_{\text{ede}}}{\epsilon_{\text{ede}}} + \frac{1}{F_{\text{ede}\to\text{ic}}} + \frac{1 - \epsilon_{\text{ic}}}{\epsilon_{\text{ic}}(1 + 2\,h_{\text{channel}}/w_{\text{channel}})} \quad [63]$$

in which $F_{\text{ede}\to\text{ic}} = F_{\text{ede}\to\text{ic,plate}} + F_{\text{ede}\to\text{ic,rib}}$.

Finally, every surface of the channel also produces a convective heat transport term q_{conv}, as discussed in the previous Section (see Eq. 52).

Computational procedure.—In order to strike a profitable balance between model accuracy and computation speed, the model equations presented in the previous Sections are solved more efficiently through the use of two specific methods.

Decoupling time-scales: First, the physical processes are assumed to proceed in three significantly different time scales. Heat transport in the solid phase is the slowest of all considered processes, and can therefore be assumed to be the only transient process when it is considered. During the solution of the heat transport problem, it can be assumed that all other processes are so fast in comparison that they can be considered to be in the steady state at any time.

Therefore, mass and energy transport in the gas phase as well as charge transport are simulated transiently only for isothermal simulations. Since charge transport is the fastest of all considered processes by orders of magnitudes, it is usually decoupled by assuming that it is always in steady state, save for the computation of EIS.

Decoupling the equations in such a way greatly reduces the computational cost of the solution procedure without significant loss in accuracy, as long as the assumptions on time-scales hold true for the computed cases.

Space-marching: Assuming a plug shape of the flow in the channel also renders the energy and mass transport in the gas flow 1D along the length of the cell (see Eqs. 4–5). In such incompressible flows with no axial diffusion, no information needs to be propagated upstream, which allows to solve this partial differential equation through space-marching. All other significant transport equations, namely mass and charge transport in the MEA, were also formulated in 1D, but in flow-normal direction: the concentration and potential gradients in the MEA are orders of magnitudes greater in this direction. Therefore, the only information needed to simulate any cross-section of the MEA is the state of the flow in upstream direction, as long as the direction of the flow is identical in both channels (co-flow configurations).
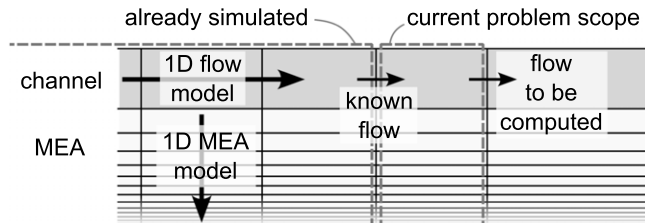

Figure 2. Illustration of the space-marching methodology.

Consequently, the problem can be solved numerically through space-marching. The partial differential equations in time and space are simplified to ordinary differential equations in time which are then solved using the semi-implicit differential-algebraic equation solver LIMEX.[53] The first discretized Section of the MEA can be solved over the full simulated time span before moving on to the next Section in flow direction. The method is illustrated in Fig. 2. It greatly reduces both simulation time and memory requirements.

This method cannot apply to the heat transport in the solid phase, since the problem is considered in 2D. However, since heat transport is decoupled from the other phenomena due to its time-scale, the space-marching algorithm can be used to compute the steady state of all other model components during each iteration of the thermal model.

Stack model.—With a functional repeating unit model, little is missing in order to be able to simulate a full SOC stack. Most importantly, SOC stack simulations require a 3D heat transport model, since significant temperature gradients can be observed in every direction. In addition, it is advantageous to be able to simulate the flow through the stack manifolds, since maldistribution of the flow to the individual cells can have a significant impact on the stack performance.[54] Flow maldistribution is an especially relevant topic in SOC stacks optimized for compactness, such as for mobile applications.[55] Finally, the potential difference under which individual cells operate is not homogeneous throughout the stack and need to be computed to accurately represent cells connected in series.

Computation procedure.—Similarly to the cell model, the stack model is accelerated by leveraging three different methods presented in this section. The resulting set of ordinary differential equations in time are also solved using the semi-implicit differential-algebraic equation solver LIMEX.[53]

Decoupling time-scales: To construct a computationally efficient SOC stack model, it is advantageous to decouple the relatively rapid chemical reactions and gas transport processes occurring within the cells from the considerably slower heat transport process taking place within the stack, just as it is done on the RU scale. In the case of stack simulations, only steady state simulations of the RUs and the flow need to be performed. These steady state simulations are performed under the assumption of a constant solid-phase temperature.

Homogenization: A SOC stack can be composed of hundreds of cells, each cell also being divided in dozens of RUs. Using a discretization as detailed as the cell model, with a matching discretization in the third dimension, would lead to impractical computation times, especially considering that the RU model has to be solved a great number of times for each iteration of the heat transport model.

Resolving the temperatures of the individual solid phases of the RUs requires a discretization in the μm scale of the MEA, while the stack's scale is oders of magnitudes larger. At the cost of losing information about the temperature differences between layers of the RUs, the cell can be homogenized and treated as a single porous material with anisotropic heat transport properties for the sake of the heat transport model at the stack scale.
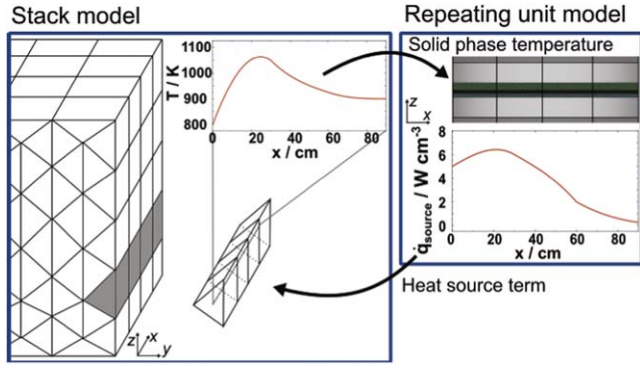
Figure 3. Schematic of the coupling between the homogenized stack heat transport model and the 1D+1D repeating unit model. A contiguous set of prismatic cells is isolated, its temperature profile extracted and passed to the RU model. In turn, the RU model is simulated and returns the spacial distribution of heat production along the RU.

The density $\rho_{\text{stack}}^{\text{eff}}$ and specific heat capacity $c_{p,\text{stack}}^{\text{eff}}$ of the lumped solid phase of the stack are computed as follows:[24]

$$\rho_{\text{stack}}^{\text{eff}} = \sum_{m \in \mathbf{M}} \alpha_{m,\text{tot}} \rho_m \qquad [64]$$

$$c_{p,\text{stack}}^{\text{eff}} = \sum_{m \in \mathbf{M}} \alpha_{m,\text{tot}} c_{p,m}. \qquad [65]$$

where $\mathbf{M}$ is the set containing all the solid phases in the stack and $\alpha_{m,\text{tot}}$ is the total volume fraction of material m.

Due to the layered geometry of planar SOCs, the spacially averaged thermal conductivity λ^{eff} needs to be anisotropic, since heat transport across the cells is slowed down by the low conductivity of the porous layers, while it is accelerated along the length and width of the cells by the interconnects. The thermal conductivity is computed according to the method elaborated by Banerjee et al.,[24] which consists of determining the total heat transfer resistance of a network of resistors each representing a separate component of the repeating units. In directions coplanar to the MEA, the resistors are arranged in parallel, while in the normal direction, the resistors are mainly arranged in series.

Using this method, the discretization does not need to take the individual RUs into account, greatly simplifying the meshing procedure. The only practical limitation is that computational cells should preferably be right prisms aligned in the same direction as the RUs. This way, a contiguous set of prismatic cells running from the inlet of the stack to the outlet can be assimilated to a RU, so that the temperature along the centerline of this set of cells can be used as constant solid-phase temperature in the RU model and the heat source terms resulting from the RU simulation can be applied to these prismatic cells in turn. This procedure is illustrated in Fig. 3, which shows how a contiguous set of prismatic cells is isolated, its temperature profile extracted and passed to the RU model. In turn, the RU model return the spacial distribution of heat production along the RU $\dot{q}_{\text{source}}^{V}(x)$.

Clustering: Each RU having their own temperature profile, gas flow rates and cell potential, it is necessary to evaluate the performance of each of them. Although the RU model may be computed for each set of contiguous computational cells, better computation speeds may be reached by re-using RU simulation results for multiple computational cells that operate under the same conditions. Such cases are very common, since stacks are usually symmetrical.

To reduce the computational load even further, a clustering algorithm is employed to group computational cells with similar, but not necessarily identical, operating conditions. For each cluster, a

single RU is simulated, and its performance is assumed to be representative of every RU within the cluster.[56,57]

Of all operating parameters of RUs, the temperatures, potentials, and inlet flow rates can vary within the stack. Therefore, RUs are clustered according to these parameters after defining a maximum absolute and relative deviation between RUs of the cluster and the representative RU.

Heat transport.—Heat transport in the stack is simulated by solving a 3D heat diffusion equation which can be formulated identically to Eq. 53:[56]

$$\rho^{\text{eff}} c_p^{\text{eff}} \frac{\partial T}{\partial t} = \nabla \cdot \lambda^{\text{eff}} \nabla T + \dot{q}_{\text{source}}^{V} \qquad [66]$$

In addition to the equation now being solved in the third dimension, its implementation also differs. Since the stack thermal model is homogenized, the source term $\dot{q}_{\text{source}}^{V}$ represents the sum of all the heat sources identified at the RU scale, averaged over the volume of the RU.

A variety of boundary conditions are supported, comprising fixed temperature, fixed or temperature-dependent heat flux and free convection in a gas. They can be applied selectively to the six outer surfaces of the stack. Free convection in a gas is modeled using empirical correlations to compute the heat transfer coefficient h_{free}.[58,59] Three different coefficients are needed, all computed from Eq. 67 but different Nusselt numbers Nu: one for vertical surfaces, one for the upper horizontal surface and one for the lower horizontal surface:

$$h_{\text{free}} = \frac{Nu}{l_{\text{char}}} \lambda_{\text{env}} \qquad [67]$$

$$f_1 = (1 + 0.671 \, Pr^{-\frac{9}{16}})^{-\frac{8}{27}} \qquad [68]$$

$$Nu_{\text{vertical}} = (0.825 + 0.387 \, Ra^{\frac{1}{6}} f_1)^2 \qquad [69]$$

$$f_2 = (1 + 0.536 \, Pr^{-\frac{11}{20}})^{-\frac{20}{11}} \qquad [70]$$

$$Nu_{\text{upper}} = \begin{cases} 0.766 \, (Ra \cdot f_2)^{\frac{1}{5}}, & \text{if } Ra \cdot f_2 \leqslant 70000 \\ 0.15 \, (Ra \cdot f_2)^{\frac{1}{3}}, & \text{otherwise} \end{cases} \qquad [71]$$

$$Nu_{\text{lower}} = 0.27 \, Ra^{\frac{1}{4}} \qquad [72]$$

with λ_{env} the thermal conductivity of the fluid surrounding the stack module and l_{char} the characteristic length, which is the height of the vertical surfaces for the sides of the stack and the surface area divided by the perimeter of the horizontal surfaces for the top and bottom of the stack.

In this study, losses to the environment through free convection and radiation is considered, resulting to a heat flux at the stack surfaces q_{surf} of

$$q_{\text{surf}} = h_{\text{free}}(T - T_{\text{env}}) + \epsilon_{\text{surf}} \, \sigma_{\text{SB}} (T^4 - T_{\text{env}}^4) \qquad [73]$$

with the emissivity of the surface of the stack module ϵ_{surf} and the Stefan–Boltzmann constant σ_{SB}.

Potential computation.—In a series connection of cells, the electrical current through every cell must be equal according to Kirschoff's law. For a given current running through the stack, the potential of every cell needs to be determined so that it results in the required current. This is realized using the Newton method, taking advantage of the fact that the polarization resistance is the derivative

of the cell potential with respect to the current:

$$E_{n+1}(t, m) = E_n(t, m) + R_n(t, m) \cdot (I_n(t, m) - I_{\text{target}}) \, k_{\text{relax}} \quad [74]$$

with $E_n(t, m)$ the n-th iteration of the potential difference across the m-th cell at time t, R the polarization resistance of the cell, I the total current flowing through the cell and k_{relax} a relaxation factor used to stabilize the scheme in difficult cases.

However, Eq. 74 is formulated for a full cell of the stack, which are not discretized as such in the homogenized model. Instead, the integral values of current $I_n(t, z)$ and resistance $R_n(t, z)$ are obtained for any vertical coordinate z by integrating the current density and area-specific resistance (ASR) over a horizontal x–y plane of the homogenized stack. This integration is performed at every vertical coordinate at which a computational cell center can be found, so that a new estimation of the homogenized potential difference field $E_{n+1}(t, z)$ can be computed:

$$E_{n+1}(t, z) = E_n(t, z) + R_n(t, z) \cdot (I_n(t, z) - I_{\text{target}}) \, k_{\text{relax}} \quad [75]$$

The current density and ASR fields, which are integrated over the x–y planes in order to obtain the current $I_n(t, z)$ and resistance $R_n(t, z)$, are obtained by solving the RU model for every computational cell (potentially accelerated through clustering) into the steady state for the current guess of $E_n(t, z)$ and interpolating the RU simulation results for every relevant x–y plane. The ASR is estimated in every computational cell by the RU model with the following equations:

$$ASR = ASR_\Omega + \frac{\eta_{\text{conc}}}{i} + \frac{\eta_{\text{act,elyt,fuel}} + \eta_{\text{act,elyt,air}}}{i} \quad [76]$$

$$\eta_{\text{conc}} = \frac{RT}{2F} \log\left(\frac{p_{\text{H}_2,\text{chan}} \, p_{\text{H}_2\text{O},\text{elyt}}}{p_{\text{H}_2,\text{elyt}} \, p_{\text{H}_2\text{O},\text{chan}}} \right) + \frac{RT}{4F} \log\left(\frac{p_{\text{O}_2,\text{chan}}}{p_{\text{O}_2,\text{elyt}}} \right). \quad [77]$$

$\eta_{\text{act,elyt,fuel}}$ and $\eta_{\text{act,elyt,air}}$ are the activation overpotentials computed with Eq. 26 directly on the surface of the electrolyte. η_{conc} is the concentration overpotential estimated from the ratios of partial pressures of the reactants in the gas channels p_{chan} and in the corresponding electrode on the surface of the electrolyte p_{elyt}. ASR_Ω is the ohmic overpotential containing the resistance of the electrolyte obtained from material properties and contact resistances which are dependent on the construction of the cell. The contact resistances are obtained while calibrating the cell model.

Equation 75 is iterated until the achieved current is within a provided tolerance of the target I_{target}. If only the steady state solution is of interest, the solution procedure can be accelerated significantly by iterating only once per time step.

Internal manifold model.—The flow through the internal manifolds of SOC stacks is modeled using a hydraulic network model based on the Bernoulli equation. With this method, the flow through channels is considered to be 1D and the relationship between pressure, velocity and the properties of the fluid is computed using the Bernoulli equation, with added terms for pressure losses through friction. Geometric features of the flow, such as the junctions between straight channels, are simply represented by pressure losses that depend on the local geometry and properties of the flow.

Such a model is comparatively fast because it consists of a limited number of algebraic equations. In its present formulation, only $4 + n_{\text{RU}}$ equations have to be solved per side of the cell (fuel and air) to compute the pressure in the inlet manifold, flow rate in the inlet manifold, flow rate through all the n_{RU} channels, pressure in the outlet manifold and flow rate in the outlet manifold. In addition, it is able to model both laminar and turbulent flow. However its accuracy relies on the quality of the expressions used to compute the pressure losses. The pressure losses considered in this model are depicted in Fig. 4.
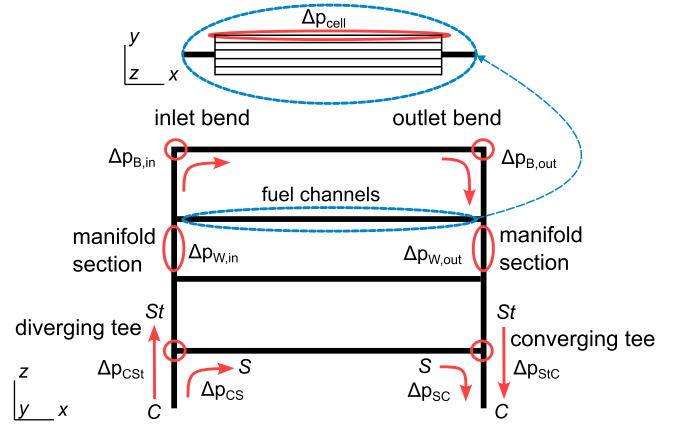

Figure 4. Schematic of the stack flow with a visualization of flow features for which the pressure losses are considered in the manifold model. The labels C, S and St are used to differentiate the common channel, side channel and straight passage of tee junctions. Adapted from Furst et al.[60]

The system of algebraic equations for a U-type manifold in a stack of n_{cells} cells, each composed of n_{RU} RUs, numbered from bottom to top with the inlet and outlet being at the bottom, is as follows:

$$\begin{cases} Q_{\text{in}}^k - \sum_{j}^{n_{\text{RU}}} Q_{\text{RU} \, j}^k = 0 & k = n_{\text{cells}} \\ Q_{\text{in}}^k - Q_{\text{in}}^{k+1} - \sum_{j}^{n_{\text{RU}}} Q_{\text{RU} \, j}^k = 0 & k \neq n_{\text{cells}} \end{cases} \quad [78]$$

$$\begin{cases} Q_{\text{out}}^k - \sum_{j}^{n_{\text{RU}}} Q_{\text{RU} \, j}^k = 0 & k = n_{\text{cells}} \\ Q_{\text{out}}^k - Q_{\text{out}}^{k+1} - \sum_{j}^{n_{\text{RU}}} Q_{\text{RU} \, j}^k = 0 & k \neq n_{\text{cells}} \end{cases} \quad [79]$$

$$\begin{cases} Q_{\text{in}}^k - Q_{\text{tot}} = 0 & k = 1 \\ p_{\text{tot,in}}^{k-1} + \Delta p_{\text{W,in}}^{k-1} + \Delta p_{\text{CSt}}^{k-1} - p_{\text{tot,in}}^k = 0 & k \neq 1 \end{cases} \quad [80]$$

$$\begin{cases} p_{\text{out}}^k - P_0 = 0 & k = 1 \\ p_{\text{tot,out}}^k - p_{\text{tot,out}}^{k-1} + \Delta p_{\text{W,out}}^{k-1} + \Delta p_{\text{StC}}^{k-1} = 0 & k \neq 1 \end{cases} \quad [81]$$

and for $j \in [1, n_{\text{RU}}]$

$$\begin{cases} p_{\text{tot,in}}^k + \Delta p_{\text{cell} \, j}^k + \Delta p_{\text{B,in}} + \Delta p_{\text{B,out}} - p_{\text{tot,out}}^k = 0 & k = n_{\text{cells}} \\ p_{\text{tot,in}}^k + \Delta p_{\text{cell} \, j}^k + \Delta p_{\text{CS}}^k + \Delta p_{\text{SC}}^k - p_{\text{tot,out}}^k = 0 & k \neq n_{\text{cells}} \end{cases}$$
$$[82]$$

with $p_{\text{tot}} = p + \rho \, u^2/2$, $p_{\text{tot,in}}^k$ and $p_{\text{tot,out}}^k$ the total pressures before and after the k-th cell, $Q_{\text{RU} \, j}^k$ the flow rate through the j-th RU of the k-th cell, $\Delta p_{\text{cell} \, j}^k$ the pressure loss across the j-th RU of the k-th cell, Δp_{CS} and Δp_{SC} the turning losses in T-junctions at the inlet and outlet of the stack, Δp_{CSt} and Δp_{StC} straight passage losses in T-junction at the inlet and outlet of the stack, $\Delta p_{\text{B,in}}$ and $\Delta p_{\text{B,out}}$ turning losses at the top of the stack, Δp_{W} the wall friction losses in a straight Section of the inlet or outlet manifold, P_0 the static pressure at the outlet of the stack and Q_{tot} the total flow rate fed to the stack.
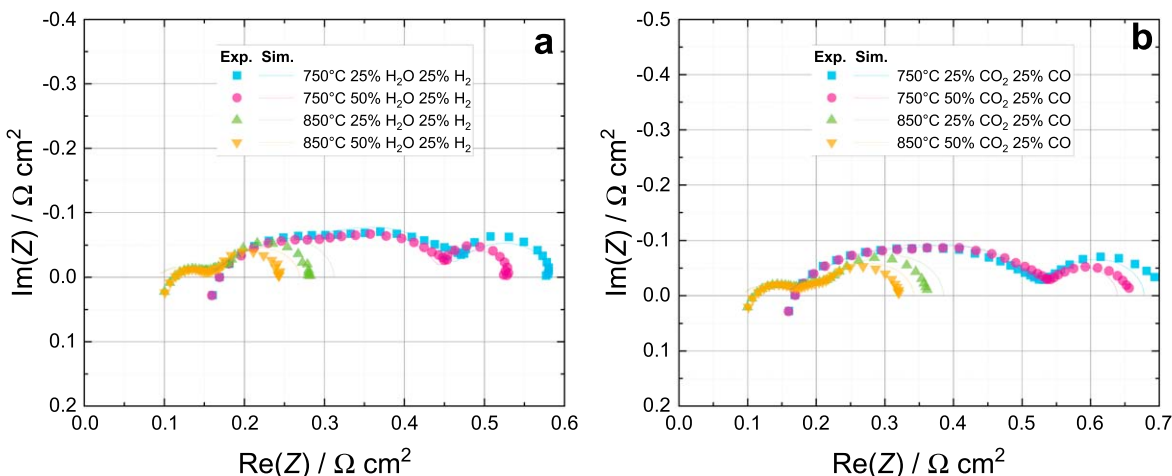
Figure 5. Fit of the button cell model to EIS of the cell of Ebbesen et al.[61] for operation with (a) H_2, H_2O and Ar and with (b) CO, CO_2 and Ar.

The system of equations is solved iteratively using the secant method. This extension of a previously published model[60] is designed to consider the flow maldistribution between the RUs of a same cell, which is caused by variations in the properties of the fluid due to temperature differences. Examples of pressure loss coefficients used to compute the pressure losses in this set of equations can be found in Eqs. 83–90.

In order to map the results of the network model to a computational cell of the homogenized stack model, especially the inlet flow velocities, a bilinear interpolation from the four closest channels to the center of the computational cell is performed. Conversely, the fluid properties inside the homogenized model are mapped to the channels of the flow model through barycentric interpolation of the three closest computational cell centers to the centerline of a channel.

Results and Discussion

Cell model parametrization.—In this section, it is explained how the model described in the previous Sections is parametrized in order to model the fuel-electrode-supported LSM-YSZ/YSZ/Ni-YSZ cell manufactured and characterized by Ebbesen, Knibbe and Mogensen.[61]

Cell structure.—In the referenced publication, the composition of the layers of the MEA and their approximate thickness is provided. Since no detailed description of the electrode microstructure is provided, some educated guesses have to be made about the exact construction of the electrodes. The supporting fuel electrode was assumed to have been manufactured as a thick but more porous support layer and a thin functional layer optimized for the electrochemical reaction. Assumed structural parameters of the cell are listed in Table I. From these parameters, the additional structural parameters required to solve the full set of differential equations is derived using the microstructure model for cermet electrodes presented before.

Electronic and ionic conductivities of common SOC materials can be found in the literature. Therefore, DETCHEM^{SOC} includes built-in expressions for the ionic and electronic conductivities of such materials, as well as the option to define custom conductivities as functions of temperature and gas partial pressures. The electrical properties of all the materials comprised in the present SOC model are listed in Table II.

EIS simulations.—The greatest advantage of a transient SOC model is the intrinsic ability to reproduce EIS, which are inherently transient. Herein, EIS are determined according to the potential step and current relaxation method outlined by Bessler.[65] EIS are a popular characterization tools for electrochemical devices because

Table I. Structural parameters of the cell assumed in this study.

Layer	Parameter	Unit	Value
Air electrode	Thickness	μm	20
	Porosity	%	35
	LSM volume fraction[a]	%	50
	YSZ volume fraction[a]	%	50
	Particle diameter	μm	1
	Tortuosity[c]	—	3.9
Electrolyte	Thickness	μm	15
Fuel electrode			
Functional layer	Thickness	μm	15
	Porosity	%	20
	Ni volume fraction[a]	%	50
	YSZ volume fraction[a]	%	50
	Particle diameter	μm	1
	Tortuosity[c]	—	21
Support layer	Thickness	μm	300
	Porosity[b]	%	32
	Ni volume fraction[a]	%	50
	YSZ volume fraction[a]	%	50
	Particle diameter	μm	10
	Tortuosity[c]	—	5.3

a) In the solid phase b) This parameter was adapted in order to reach the correct concentration overpotentials. c) Computed according to Eq. 46

Table II. Conductivities of the SOC materials used in this study.

Material	Electronic conductivity σ_{el} S cm^{-1}	Ionic conductivity σ_{io} S cm^{-1}	References
Ni	$32700 - T \cdot 10.653\ \mathrm{K}^{-1}$	—	62
YSZ	—	$334\, e^{-\frac{10300\ \mathrm{K}}{T}}$	63
LSM	$\frac{885500\ \mathrm{K}}{T} e^{\frac{-9000\ \mathrm{J\,mol}^{-1}}{RT}}$	—	64
Crofer 22H	$6950\, e^{\frac{307.7\ \mathrm{K}}{T}}$	—	14

they provide information about individual physical phenomena, instead of characterizing the overall performance of the cell. While polarization curves allow to measure the ASR of a cell as a

Table III. Parameters of the electrochemical model.

Reaction	Exchange current density i_0/A cm^{-1}	Charge-transfer coefficients	
		β_a	β_c
OER/ORR	$3 \cdot 10^6 \exp\left(-\frac{253769 \ \text{J mol}^{-1}}{R\,T}\right) \frac{p_{O_2}}{1 \ \text{Pa}}^{0.18}$	0.5	1.5
HOR/H$_2$ORR	$250 \exp\left(-\frac{160000 \ \text{J mol}^{-1}}{R\,T}\right) \frac{p_{H_2}}{1 \ \text{Pa}}^{-0.1} \frac{p_{H_2O}}{1 \ \text{Pa}}^{0.33}$	0.5	0.5
COOR/CO$_2$RR	$7 \cdot 10^3 \exp\left(-\frac{180000 \ \text{J mol}^{-1}}{R\,T}\right) \frac{p_{CO}}{1 \ \text{Pa}}^{0.25} \frac{p_{CO_2}}{1 \ \text{Pa}}^{-0.25}$	1.5	0.5

function of its polarization, an EIS allows to distinguish how much of the ASR is due to the electrochemical reaction kinetics, as opposed to mass transport inhibition.[66] Therefore, EIS are an invaluable tool for the calibration of cell models.

Despite the described modeling methodology being fully parametrized by physical parameters, some physical properties of SOC cannot be measured directly and need to be determined through fitting of simulation results to the experiments. This is typically the case for the coefficients of the Butler-Volmer equation, such as activation energy and pre-exponential factors in the exchange current density.

Reproducing experiments from literature also often requires determining some of the microstructural properties of the cell through fitting, since this data is often not included in publications. In the present case, reproducing the experiments of Ebbesen et al.,[61] only electrode thicknesses are provided and at least the support layer porosity needs to be determined due to its large impact on concentration overpotentials.

Fortunately, despite the multitude of fitted variables, calibrating the cell model on EIS prevents overfitting in multiple ways:

1. The contributions of polarization resistance, ohmic resistance and mass transport inhibition on the total cell ASR can be fitted individually.
2. The double-layer capacitance of an electrode has no influence on the local activation overpotential, only on the frequency response. The capacitance and exchange current density can therefore be fitted independently.
3. The very thin electrodes, such as the oxygen electrode in the present cell, have a minor influence on mass transport. In electrode-supported cells, the porosity and tortuosity of the support layer have a dominant influence on concentration overpotentials. In such cases where nothing of the cell microstructure is known, the microstructure of thin layers may thus be guessed without introducing significant errors, and the concentration overpotentials fitted solely based on the support layer.
4. Theoretically, the triple phase boundary length λ^V_{TPB} of the electrodes have a major impact on the cell performance, but in practice, this parameter cannot be separated from the exchange current density pre-exponential factor through fitting (see Eq. 22). When fitting the pre-exponential factor of the exchange current density, it is actually the product of pre-exponential factor and triple phase boundary length (or electrode/gas boundary area in the case of mixed electronic-ionic conducting electrodes) which is fitted.

Figure 5 depicts the finalized cell model compared to the experimental EIS data of Ebbesen et al.[61] Overall, the agreement between the model and the experiments is excellent.

As outlined by the authors of the experimental study, the open circuit voltage (OCV) observed during the experiments is different than the OCV computed from the gas compositions, which is likely the result from a gas or current leak through the MEA. Herein, it was assumed to be fully caused by a current leak and an electronic

conductivity of $0.4 \exp\left(\frac{-9500}{T}\right)$ S cm^{-1} in the electrolyte was found to accurately reproduce the measured OCV.

The ohmic resistance of the cell, determined by the real part of the leftmost point of the spectrum, can be reproduced with great accuracy. Only a small contact resistance of 0.045 Ω cm^2 was determined through fitting, while literature data for material conductivities accounts for most of the ohmic ASR. On the experimental EIS plots, the high frequency data points exhibit a positive imaginary part, which is only due to the inductance of the measurement setup,[67] and is therefore not desired in the cell model. Since such an inductance does not contribute to the cell resistance, it does not impact the fitting procedure significantly.

An excellent fit was also achieved on the activation overpotentials. This requires fitting a greater number of values, namely the pre-exponential factor, activation energy and pressure exponents of the exchange current densities. Fortunately, the experimental dataset includes experiments at different temperatures, allowing to fit the activation energy, and different partial pressures in the feed gas, allowing to fit the pressure exponents reliably. These parameters need to be determined independently for the oxygen evolution reaction/oxygen reduction reaction (OER/ORR), hydrogen oxidation reaction/water reduction reaction (HOR/H$_2$ORR) and CO oxidation reaction/CO$_2$ reduction reaction (COOR/CO$_2$RR) independently, which is fortunately not too challenging since they can be distinguished as significantly distinct arcs in the EIS. The fitted exchange current densities are listed in Table III. The charge transfer coefficients β_a and β_c are the last remaining parameters of the Butler-Volmer equation that need to be fitted, but their influence is most noticeable at higher current densities. Therefore, in the absence of EIS measured under higher polarization, the present charge transfer coefficients were fitted using polarization curves, although the simulation results were noted to be rather insensitive to changes in charge transfer coefficients.

Finally, a satisfactory fit was achieved regarding concentration overpotential by fitting the fuel electrode support layer porosity. However, a slight mismatch in the influence of the temperature on the low frequency arc can be observed, as the concentration overpotential is slightly overestimated at high temperatures. This is likely due to the low flow rate of 20 sL/h used in the experiments, which is inconsistent with the assumption of perfectly mixed gas phase above the electrode. This suggests the need for a more detailed gas compartment model.

Due to the wealth of experimental data available, four datasets could be conserved as validation data. These remaining experiments all include gases that react on the surface of the nickel electrode, so that the heterogeneous chemistry model needs to be activated in those cases. A 42-step elementary reaction mechanism for methane reforming and water-gas shift on Ni-YSZ is used.[39] It provides 42 reaction rate equations for the thermocatalytic heterogeneous chemistry model (expressed in generic form as Eq. 19), which in turn influences species conservation through the species production rate $\dot{s}_m$ of Eq. 15. No additional calibration is needed. Comparison between experiments and simulations is shown in Fig. 6.
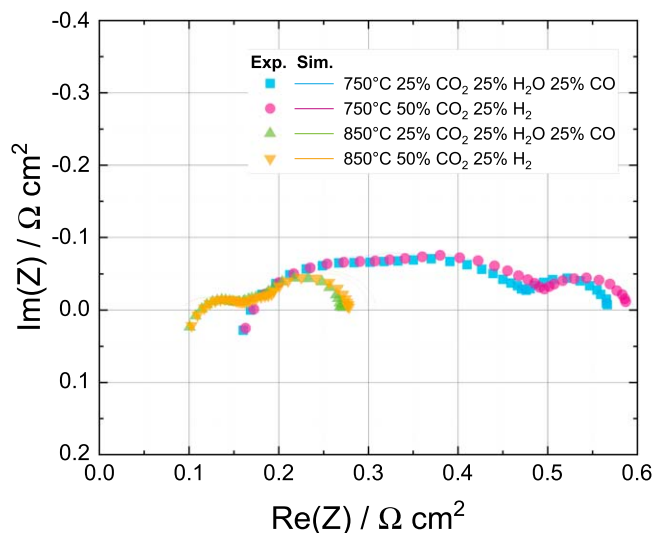
Figure 6. Fit of the button cell model to EIS of the cell of Ebbesen et al.[61] under conditions with mixed HOR/H$_2$ORR and COOR/CO$_2$RR charge-transfer reactions and thermocatalytic surface reactions on the Ni-YSZ electrode.

Figure 7. Fit of the button cell model to experimental polarization curves of Ebbesen et al.[61] under conditions with mixed HOR/H$_2$ORR and COOR/CO$_2$RR charge-transfer reactions and thermocatalytic surface reactions on the Ni-YSZ electrode.

The agreement between experiments and simulations on this validation dataset is very good, and showcases that the mixed H$_2$O/CO$_2$ electrolysis model works without need for additional fitting or other special treatment. In addition, the heterogeneous chemistry model is also demonstrated to work adequately in this case, although a case that is more strongly influenced by surface reaction kinetics would be required for proper testing, as the low flow rates used in the experimental setup lead to a composition of the gas phase close to equilibrium in the active layer of the fuel electrode.

Validation of polarization curves.—While the EIS data is the most useful for fitting the unknown parameters of the model, the polarization curves remain a useful tool to verify the adequacy of the fitted parameters under different polarization conditions, especially since the published dataset on which the present model is based provides only EIS measured at OCV, which is common practice. Comparison between simulated polarization curves and the experimental data of Ebbesen et al.[61] under conditions with mixed H$_2$ORR/HOR and CO$_2$RR/COOR charge-transfer reactions and surface reactions on the Ni-YSZ electrode is shown in Fig. 7.

Excellent agreement between the simulated and experimental polarization curves is reached for all cases over most of the simulated potential range. Notably, the OCV is predicted reliably despite the current leakage. The agreement is weakest at high current densities, negative and positive, which is where concentration overpotential dominates the losses in the cell. This is congruent with the flow model at the surface of button cells showing larger errors at low flow rates, as identified in the previous section.

Overall, this verification step confirms the ability to calibrate the cell model using solely EIS measured at OCV.

Stack model parametrization.—In this study, a stack of the LSM-YSZ/YSZ/Ni-YSZ cells is considered, on which the cell model was calibrated in the previous section.

A stack of 40 cells with an active area of 90×175 cm^2 is considered. In this arrangement, the number of cells in the stack is high enough so that flow maldistribution due to friction losses in the manifold can be expected, but not high enough to have turbulent flow in parts of the manifolds under reasonable operating conditions.

The interconnects are assumed to be made of Crofer 22 H, and the stack is insulated on all sides by a 5 cm layer of the Promalight-1000X material. The effect of the gaps in the insulation due to the
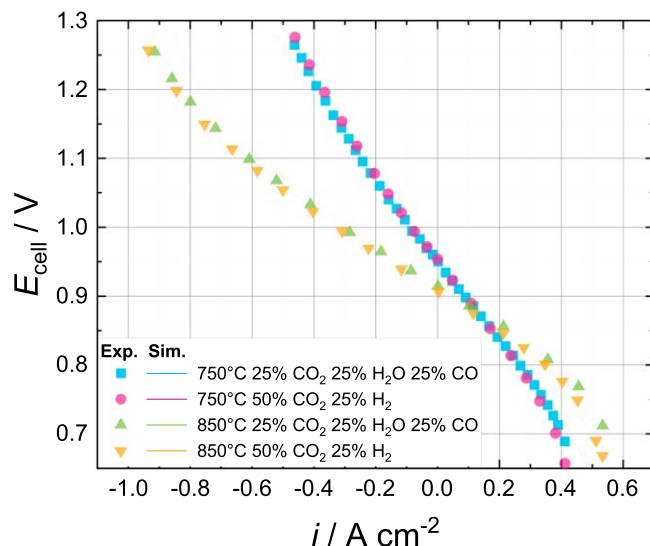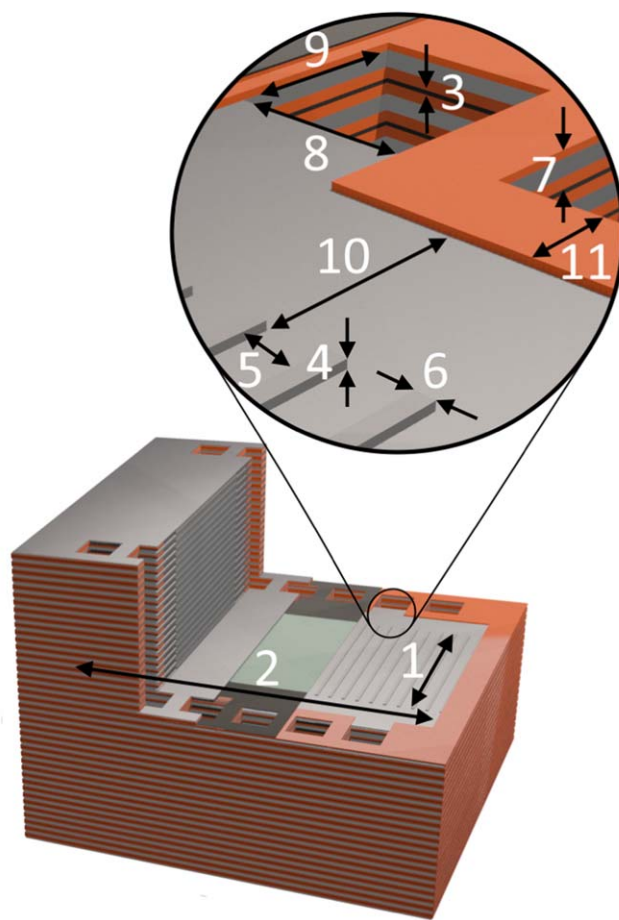

Figure 8. Sectional view of the SOC stack showing the geometry of the interconnects (in gray), sealing gaskets (in orange) and the SOC (in green) in its guide frame (in black). Measurements are annotated according to the numbered labels of Table IV.

inlets and outlets of the manifolds is neglected. The electric conductivity of Crofer 22 H is shown in Table II, and no additional contact resistance was considered.

Table IV. Dimensions of the SOC stack. The dimensions of the manifold are adopted from a prior publication presenting a flow model for this specific geometry.[60]

#	Dimension	Value	Unit
1	Cell length	90	mm
2	Cell width	175	mm
3	MEA thickness	350	μm
4	Air and fuel channel height	1	mm
5	Air and fuel channel width	4.75	mm
6	Interconnect rib width	1.5	mm
7	Interconnect total height	4.1	mm
8	Manifold channel width	17	mm
9	Manifold channel depth	17	mm
10	Inlet & outlet header length	17	mm
11	Sealing width	8	mm

Table V. Thermal properties of the stack components. Their values were assumed to be constant and evaluated at 1100 K.

Material	Specific heat capacity c_p J/kg/K	Thermal conductivity λ W/m/K	Density ρ kg/m³	References
Ni	561.0	68.1	8900	68, 69
YSZ	620	2.1	5938	70, 71
LSM[a]	610	3.4	6300	72, 73
Crofer 22H	660	26.1	7800	14, 74
Promalight-1000X	1070	0.036	280	75

a) In the absence of published data, the thermal properties of LSM were assumed to be similar to those of LSCF.

The geometry of the stack is illustrated in Fig. 8 and measurements are provided in Table IV. The thermal properties of all the materials comprised in the SOC stack are listed in Table V.

The pressure loss coefficients, required to characterize the geometry of the stack manifold in the flow model (Eqs. 78–82), are computed using the expressions listed as Eqs. 83–90 uncovered in a previous study.[60]

$$\zeta_{CSt} = \frac{\overline{p}_{tot,St} - \overline{p}_{tot,C}}{\rho \overline{u}_{z,C/2}^2}$$
$$\approx 39.67 \left(\frac{Q_S}{Q_C} \right)^2 \frac{Q_{St}}{Q_C} - 0.4069 \qquad [83]$$

$$\zeta_{CS} = \frac{\overline{p}_{tot,S} - \overline{p}_{tot,C}}{\rho \overline{u}_{z,C/2}^2}$$
$$\approx -\frac{Q_S/Q_C}{Re_C}(226 Re_S + 3574) - 0.9842 \qquad [84]$$

$$\zeta_{StC} = \frac{\overline{p}_{tot,C} - \overline{p}_{tot,St}}{\rho \overline{u}_{z,C/2}^2}$$
$$\approx \frac{Re_S Q_C/Q_{St} + 15.59/Re_S - 14.79}{Re_C Q_{St}/Q_C} \qquad [85]$$
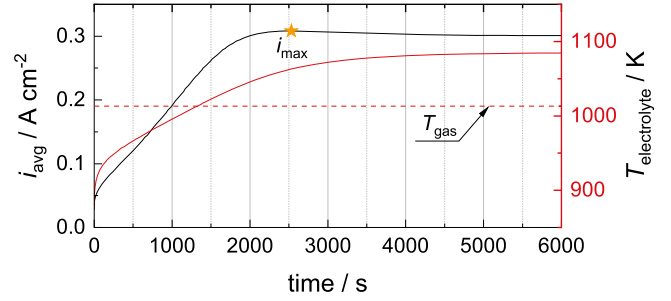
Figure 9. Evolution over time of the average electrolyte temperature and current density in a repeating unit starting at a constant temperature of 873 K being fed with humidified ammonia and air at 1023 K under a potential of 0.8 V.

$$\zeta_{SC} = \frac{\overline{p}_{tot,C} - \overline{p}_{tot,S}}{\rho \overline{u}_{z,C/2}^2} \approx \frac{2845 \, Q_S/Q_C}{1.01 - Re_C} + 0.7872 \qquad [86]$$

$$\zeta_{B,in} = \frac{\overline{p}_{tot,cell,in} - \overline{p}_{tot,M_{in}}}{\rho \overline{u}_{z,M_{in}/2}^2} \approx -5727/Re_{M_{in}} \qquad [87]$$

$$\zeta_{B,out} = \frac{\overline{p}_{tot,M_{out}} - \overline{p}_{tot,cell,out}}{\rho \overline{u}_{z,M_{out}/2}^2} \approx -4702/Re_{M_{out}} \qquad [88]$$

$$f_{D,in} = \frac{63.13}{Re_M} \left(Re_{cell} \frac{z}{h_{tot}} + 0.3544 - \frac{z}{h_{tot}} \right) \qquad [89]$$

$$f_{D,out} = \frac{31.47}{Re_M} (Re_{cell} + 1.4735). \qquad [90]$$

Pressure losses in the channels are evaluated using analytical solutions for Poiseuille flow in rectangular channels.[76]

Simulation of the start-up of ammonia-fed repeating units.— Since no cell-specific calibration is needed for the heterogeneous chemistry model as long as the catalyst surface area is known or estimated well, it is possible to study the performance of the cell when it is fueled with ammonia by simply adopting a validated mechanism for ammonia decomposition on Ni-YSZ for from the literature such as the thermodynamically consistent 6-step elementary kinetic mechanism from Appari et al.[77]

The performance of a perfectly insulated RU fed with 0.65 sL/h mixture of 97% NH₃/3% H₂O at 1023 K is discussed in this section. The cell is operated at 0.8 V, in which case it reaches a fuel conversion of approximately 90%. 6.5 sL/h of 79% N₂/21% O₂ is fed to the air channel.

Figure 9 depicts the evolution of the average current density and MEA average temperature in the cell during the start up process, starting from a pre-heated cell at 873 K. Initially, the cell heats up through heat transport from the hot gas to the MEA and a small amount of resistive heating due to the electric conductivity of the MEA. Once the MEA reaches a sufficient ionic conductivity, the electrochemical reaction starts contributing to the temperature rise of the cell. In the steady state, the gas flow cools down the cell which produces heat through resistive heating and the electrochemical reactions. Ammonia cracking, which is an endothermic reaction, also helps to cool down the cell at high temperatures.

Interestingly, the highest average current density is not reached in the steady state where the average electrolyte temperature is highest. Therefore, the performance of the RU once it reaches steady
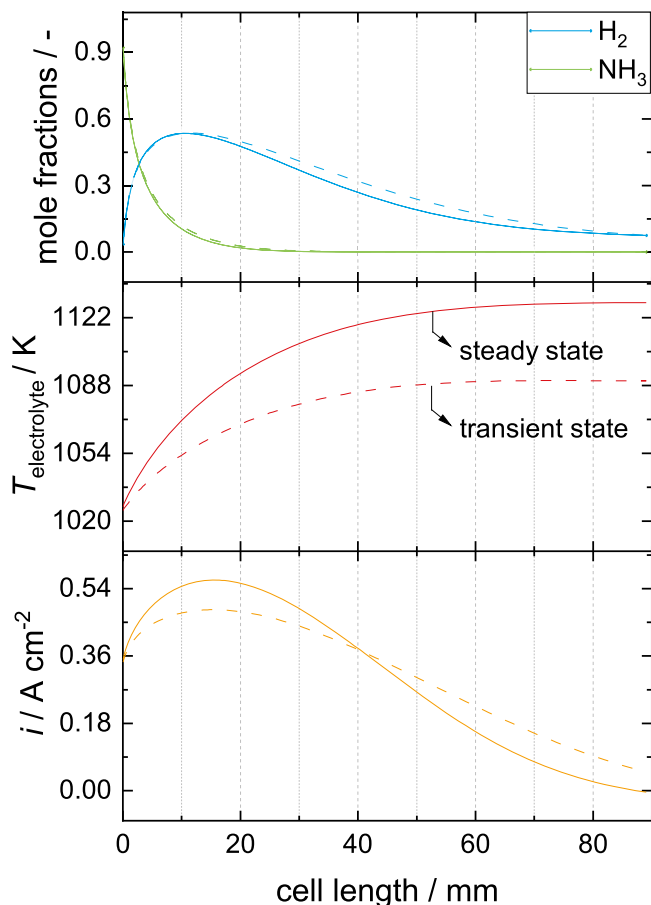
Figure 10. Axial current density, fuel channel species mole fraction and MEA temperature profiles of a RU fed with 0.65 sL/h mixture of 97% NH₃/3% H₂O at 1023 K under 0.8 V. Continuous lines represent the steady state while the dashed lines represent the state of highest current density during the heat-up of the cell.

operating conditions is studied in further detail and compared to its performance at its peak current density through the axial profiles of the MEA temperature, current density and gas channel species concentrations depicted in Fig. 10.

In the steady state, studying the species mole fractions reveals that ammonia is decomposed rapidly as soon as it enters the cell, allowing for a high current density right from the inlet. Still, as the hydrogen concentration continues to increase, so does the current density. However, the highest current density is not reached where the hydrogen concentration is highest. Since the temperature of the cell increases over its length due to the exothermic electrochemical reaction, so does the activity of the cell. Therefore, the highest current density, 0.56 A/cm^2, is reached approximately 17 mm into the cell, while the cell has reached a higher temperature but the hydrogen concentration is still high.

At the end of the cell, the current density drops to 0 A/cm^2 as the equilibrium potential reaches 0.8 V due to the low hydrogen concentration and high temperature. At this point, a hydrogen conversion of 89.8% is achieved. At the outlet, both the electrolyte and gas temperature reaches 1130 K, with the highest temperature gradient in the electrolyte being 14.2 K/mm directly at the inlet.

At the point in time where the maximum current density is reached, the MEA is significantly cooler, with a maximum temperature of 1090 K at the end of the cell. The decreased temperature toward the inlet leads to a lower peak current density where the hydrogen concentration is high, likely due to the increased ohmic overpotential. However, the lower temperature toward the outlet compared to the steady state ensures that the equilibrium potential does not drop too strongly. The current density does not drop to zero at the outlet and on average a slightly higher current density is achieved.

In order to provide a better understanding of the chemical reactions inside of the anode, the gas composition and catalyst surface coverage is shown in Fig. 11 at the inlet of the cell, at the 10 mm mark where the hydrogen concentration reaches its maximum and at the end of the cell. Therein, the active layer of the electrode can be clearly distinguished from the support layer by the sudden change in mole fraction gradients at a depth of 300 μm caused by the increased catalytic surface area. At the inlet of the cell, the high ammonia decomposition rate results in an increase in hydrogen mole fraction even close to the electrolyte, in spite of the competing electrochemical reaction. With the decreasing ammonia fraction along the channel length, this trend quickly inverts. At first, the hydrogen mole fraction increases throughout the support layer and decreases inside of the active layer. Once the maximum hydrogen fraction in the channel is achieved, approximately 10 mm from the inlet, the flow of hydrogen inverts and its mole fraction decreases monotonously over the thickness of the anode.
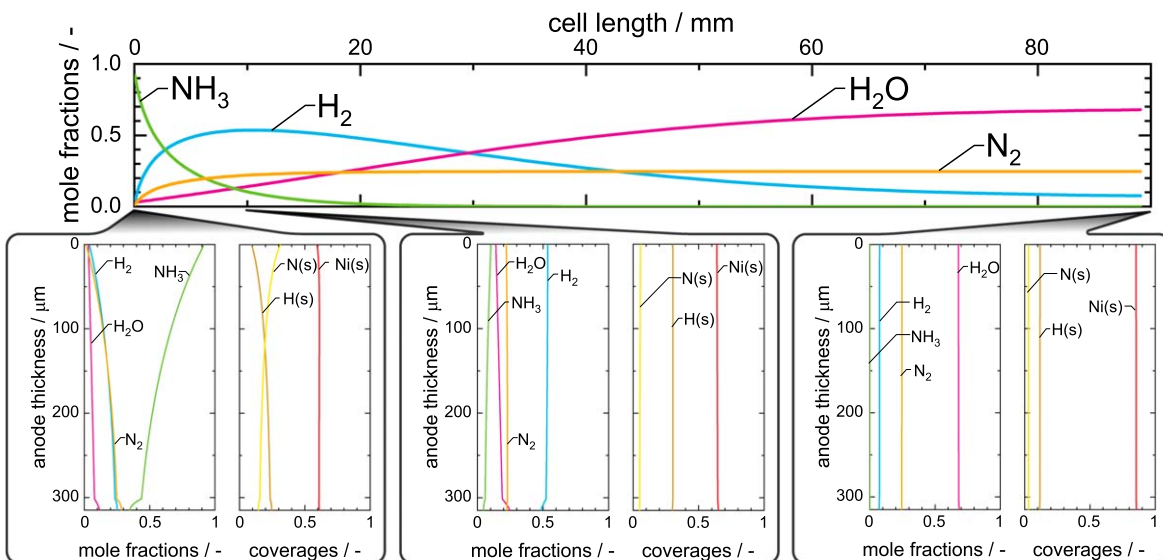

Figure 11. Gas species mole fractions along the length of the fuel channel at the steady state, accompanied by mole fractions and surface coverages through the thickness of the anode at the inlet, 10 mm from the inlet and at the end of the cell.
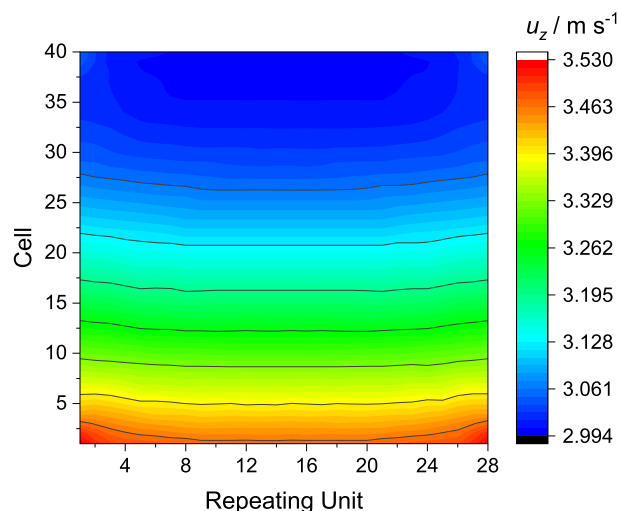
Figure 12. Contour plot of the inlet flow velocity of the air channels through all the repeating units of the stack.

Figure 11 also reveals good coverage of the Ni surfaces by N(s) and H(s) at the inlet, while the coverages by NH_3(s), NH_2(s) and NH(s) were not depicted because they are negligible due to their fast reaction rates. While the coverage by N(s) decreases as the ammonia depletes along the channel and through the anode, the coverage by H(s) is instead more greatly influenced by the hydrogen concentration. The increase in open Ni(s) sites toward the end of the channel seems therefore to be a result of the fuel depletion as well as the increased temperature.

Evaluation of the influence of flow maldistribution on stack performance.—By virtue of the stack flow model described by Eqs. 78–82, the influence of the manifold on the performance of a stack of 40 cells of the type manufactured by Ebbesen et al.[61] can be studied. The geometry of the stack considered herein was described in Table IV.

In this section, the analysis is performed on an electrolysis stack fed with a steam mixture of 90 vol% H_2O and 10 vol% H_2 at 1023 K. The fuel flow rate is adjusted to an average 7.78 sL/h, which amounts to a total fuel flow rate to the stack of 8709 sL/h, distributed to the individual channels according to the manifold model. A mixture of 21 vol% O_2 and 79 vol% N_2 is fed to the air channels with an average flow rate per channel of 15.6 sL/h, a relatively high sweep gas flow rate used for temperature management. The stack is operated at an average current density of -2.11 A cm^{-2} in the active area, resulting in an average cell potential of 1.40 V and a steam conversion rate of 72.5%. Of the achieved current density of -2.11 A cm^{-2}, -0.10 A cm^{-2} does not contribute to the electrolysis process due to the current leak of the electrolyte observed previously.

This shows that high current densities may be achieved with the present cell architecture under optimized operating conditions. However, such operating conditions also accelerate the degradation of the cell, which must be studied experimentally or with complementary simulation methods. In addition, the scale-up of single cells to full stacks introduces multiple engineering challenges such as ensuring good electrical contact between electrodes and interconnects, as well as preventing gas leakage. In the present simulation, no additional contact resistance nor gas leakage was introduced.

The flow distribution to the individual air channels of the stack is shown through a contour plot of the velocity at the inlet of the repeating units in Fig. 12. Therein, flow maldistribution is noticeable both in the vertical and horizontal direction.

Flow maldistribution along the height of the SOC stack can be expected due to the geometry of a U-type manifold such as the one studied herein. The previous study on an isothermal flow using an identical stack geometry showed that the friction inside the manifold
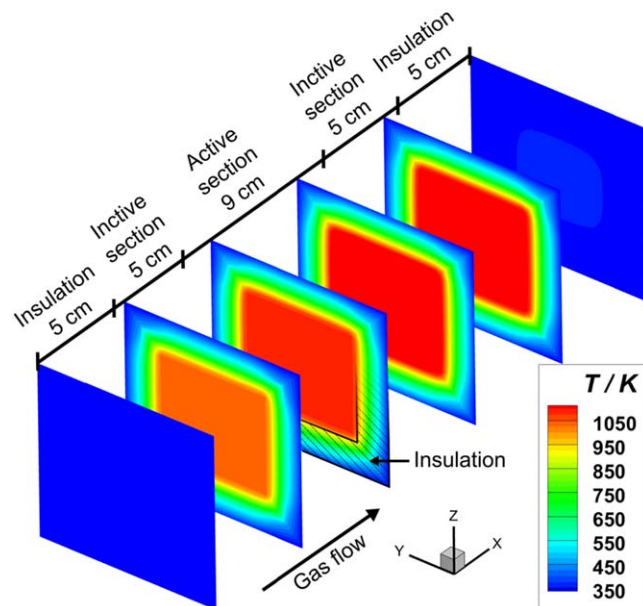

Figure 13. Temperature profiles of the SOEC stack at steady state. 5 equidistant slices are taken from the front to the back of the stack and the x-axis is stretched by a factor 3 for a better visualization.

generally causes a decrease in flow rates through cells more distant from the inlet of the manifold.[60] However, in the present case, the temperature distribution observed in Fig. 13 also introduces a slight maldistribution in the horizontal direction in which no geometric pressure losses are considered. Since the viscosity of gases increase with temperature, the flow in the central, hotter region of the stack suffers from an increased hydraulic resistance. Conversely, the highest flow velocities are found in the coldest corners of the stack.

In the present case, maldistribution in the vertical direction, which is mostly due to the manifold geometry, is much larger in scale than the maldistribution in horizontal direction which is solely due to the temperature distribution.

The temperature distribution in the stack is depicted in Fig. 13. The temperature within the stack increases by 75 K over the active area in flow direction while the temperature gradients in other directions are negligible in comparison. This is due to the highly exothermic operation of the stack, with the gases in the channel outlets 121 K above the inlet temperature on average.

Comparison with a simulation using homogeneous flow distribution shows no significant change in temperature distribution nor in conversion rate, despite a variation of 18% in sweep gas velocity. Fuel maldistribution has a magnitude of only 4% and the results indicate that it is not enough to meaningfully impact the stack performance through concentration overpotentials. As can be seen in the plot of cell potentials along the height of the stack shown in Fig. 14, only minute differences in cell performance are caused by
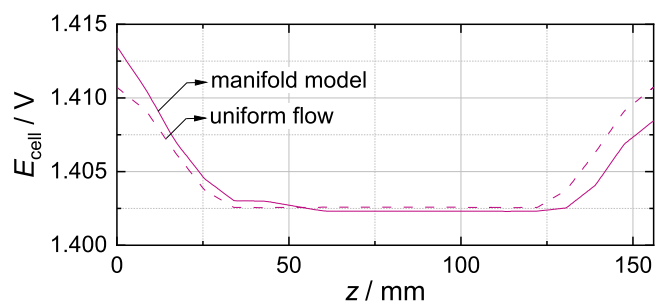

Figure 14. Cell potentials as a function of the height of the stack. The stack simulation with manifold model is compared to a simulation with uniform flow distribution.

the flow maldistribution in this case. Even then, the loss in performance at the bottom of the stack, manifested through an increase in cell potential of 3 mV in order to reach a current density of -2.11 A cm^{-2}, is compensated by an equivalent increase in cell performance at the top. The averages of cell potentials is therefore only different by 0.06 mV, or 0.004%.

Conclusions

The multi-scale framework for the transient simulation of solid oxide button cells, repeating units and stack modules integrated in DETCHEM was presented. This model was shown to effectively bridge the gap between button cell experiments and performance predictions of large-scale stacks, providing a comprehensive tool for analyzing SOC performance under various operating conditions.

The workflow of using such a model was demonstrated, starting with the calibration and validation using experimental EIS and polarization curves of a Ni-YSZ/YSZ/LSM-YSZ button cell followed by a performance analysis of the scaled-up repeating unit and stack.

The versatility of the tool was demonstrated by providing EIS of button cells, replicating experiments with both common fuel-side electrochemical reactions, validating the model on experimental data of a case that includes thermocatalytic chemistry, performing transient simulations of repeating units and simulating the flow maldistribution and potential field in a stack module.

The main shortcomings of the presented methodology is the limited geometry it is able to model. Tubular cells, as well as cross-flow and counter-flow stack configurations are widespread, but cannot yet be simulated by DETCHEM^{SOC}. In addition, the simplified geometry assumed by a two-dimensional cell model and homogenized stack model induces a loss of information on small-scale phenomena caused by tree-dimensional geometrical features.

The multi-scale SOC modeling framework integrated in DETCHEM not only enhances our understanding of cell performance but also paves the way for the scale-up of the SOC technology. By bridging the gap between experimental data and large-scale applications, such models stand as pivotal tools for researchers and engineers alike. The demonstrated versatility and robustness of the framework underscore its potential to drive innovation and optimize SOC systems for a wide range of industrial applications.

Acknowledgments

ORCID

Oscar Furst ⬤ https://orcid.org/0009-0007-7772-3660
Olaf Deutschmann ⬤ https://orcid.org/0000-0001-9211-7529

References

1. P. R. Shukla et al., *IPCC, 2022: Climate Change 2022: Mitigation of Climate Change. Contribution of Working Group III to the Sixth Assessment Report of the Intergovernmental Panel on Climate Change* (Cambridge University Press) (2022).
2. A. Hauch, R. Küngas, P. Blennow, A. B. Hansen, J. B. Hansen, B. V. Mathiesen, and M. B. Mogensen, "Recent advances in solid oxide cell technology for electrolysis." *Science*, **370**, eaba6118 (2020).
3. *Topsoe A/S Herning SOEC Manufacturing Facility*, Accessed 02.06.2024.
4. *Bloom Energy Demonstrates Hydrogen Production with the World's Most Efficient Electrolyzer and Largest Solid Oxide System* (2023), Accessed 02.06.
5. "Sunfire - World's largest high-temperature electrolyzer achieves record efficiency." Accessed 02.06.2024.
6. F. Safari and I. Dincer, "Assessment and optimization of an integrated wind power system for hydrogen and methane production." *Energy Conversion and Management*, **177**, 693 (2018).
7. C. Drechsler and D. W. Agar, "Intensified integrated direct air capture - power-to-gas process based on H$_2$O and CO$_2$ from ambient air." *Applied Energy*, **273**, 115076 (2020).
8. Y. Chi, Q. Hu, J. Lin, Y. Qiu, S. Mu, W. Li, and Y. Song, "Numerical simulation acceleration of flat-chip solid oxide cell stacks by data-driven surrogate cell submodels." *Journal of Power Sources*, **553**, 232255 (2023).
9. Y. Chi, K. Yokoo, H. Nakajima, K. Ito, J. Lin, and Y. Song, "Optimizing the homogeneity and efficiency of a solid oxide electrolysis cell based on multiphysics simulation and data-driven surrogate model." *Journal of Power Sources*, **562**, 232760 (2023).
10. L. Wang, M. Pérez-Fortes, H. Madi, S. Diethelm, J. V. herle, and F. Maréchal, "Optimal design of solid-oxide electrolyzer based power-to-methane systems: A comprehensive comparison between steam electrolysis and co-electrolysis." *Applied Energy*, **211**, 1060 (2018).
11. M. A. Khaleel, Z. Lin, P. Singh, W. Surdoval, and D. Collin, "A finite element analysis modeling tool for solid oxide fuel cell development: coupled electro-chemistry, thermal and flow analysis in MARC®." *Journal of Power Sources*, **130**, 136 (2004).
12. S. B. Beale, H.-W. Choi, J. G. Pharoah, H. K. Roth, H. Jasak, and D. H. Jeon, "Open-source computational model of a solid oxide fuel cell." *Comput. Phys. Commun.*, **200**, 15 (2016).
13. J. D. Duhn, A. D. Jensen, S. Wedel, and C. Wix, "Optimization of a new flow design for solid oxide cells using computational fluid dynamics modelling." *Journal of Power Sources*, **336**, 261 (2016).
14. L. Wehrle, Y. Wang, P. Boldrin, N. P. Brandon, O. Deutschmann, and A. Banerjee, "Optimizing solid oxide fuel cell performance to Re-evaluate its role in the mobility sector." *ACS Environmental Au*, **2**, 42 (2022).
15. A. Donazzi, S. De Pascali, F. Garavaglia, and M. Bracconi, "A quasi 2D model for the interpretation of impedance and polarization of a planar solid oxide fuel cell with interconnects." *Electrochimica Acta*, **365**, 137346 (2021).
16. J. Fan, J. Shi, R. Zhang, Y. Wang, and Y. Shi, "Numerical study of a 20-cell tubular segmented-in-series solid oxide fuel cell." *Journal of Power Sources*, **556**, 232449 (2023).
17. H. Zhu, R. J. Kee, V. M. Janardhanan, O. Deutschmann, and D. G. Goodwin, "Modeling elementary heterogeneous chemistry and electrochemistry in solid-oxide fuel cells." *J. Electrochem. Soc.*, **152**, A2427 (2005).
18. A. Banerjee and O. Deutschmann, "Elementary kinetics of the oxygen reduction reaction on LSM-YSZ composite cathodes." *J. Catal.*, **346**, 30 (2017).
19. H. Zhu and R. J. Kee, "Modeling protonic-ceramic fuel cells with porous composite electrodes in a button-cell configuration." *J. Electrochem. Soc.*, **164**, F1400 (2017).
20. J. A. Ortiz-Corrales and J. Otomo, "Simulating transport of charged defects in BaZr$_{0.8}$Y$_{0.2}$O$_{3-\delta}$|BaZr$_{0.1}$Ce$_{0.7}$Y$_{0.1}$Yb$_{0.1}$O$_{3-\delta}$ bilayer electrolytes using a Nernst-Planck-Poisson model." *Solid State Ionics*, 116680 (2024).
21. O. Deutschmann et al., *DETCHEM* (2022), Accessed 05.06.2024.
22. *DETCHEM-Mechanisms*, Accessed 05.06.2024.
23. V. Menon, Q. Fu, V. M. Janardhanan, and O. Deutschmann, "A model-based understanding of solid-oxide electrolysis cells (SOECs) for syngas production by H$_2$O/CO$_2$ co-electrolysis." *Journal of Power Sources*, **274**, 768 (2015).
24. A. Banerjee, Y. Wang, J. Diercks, and O. Deutschmann, "Hierarchical modeling of solid oxide cells and stacks producing syngas via H$_2$O/CO$_2$ Co-electrolysis for industrial applications." *Applied Energy*, **230**, 996 (2018).
25. L. Wehrle, D. Schmider, J. Dailly, A. Banerjee, and O. Deutschmann, "Benchmarking solid oxide electrolysis cell-stacks for industrial Power-to-Methane systems via hierarchical multi-scale modelling." *Applied Energy*, **317**, 119143 (2022).
26. S. E. Bechtel and R. L. Lowe, *Fundamentals of continuum mechanics: with applications to mechanical, thermomechanical, and smart materials* (Academic Press, an imprint of Elsevier, Amsterdam Boston) (2015).
27. L. L. Raja, R. J. Kee, O. Deutschmann, J. Warnatz, and L. D. Schmidt, "A critical evaluation of navier-stokes, boundary-layer, and plug-flow models of the flow and chemistry in a catalytic-combustion monolith." *Catal. Today*, **59**, 47 (2000).
28. R. J. Kee, M. E. Coltrin, P. Glarborg, and H. Zhu, *Chemically Reacting Flow: Theory, Modeling, and Simulation* (Wiley) 1 ed. (2017).
29. M. S. Day and J. B. Bell, "Numerical simulation of laminar reacting flows with complex chemistry." *Combust. Theory Modelling*, **4**, 535 (2000).
30. H. Zhu and R. J. Kee, "Modeling electrochemical impedance spectra in SOFC button cells with internal methane reforming." *J. Electrochem. Soc.*, **153**, A1765 (2006).
31. E. A. Mason and A. P. Malinauskas, *Gas Transport in Porous Media: The Dusty-gas Model* (1983), Chemical engineering monographs 17 (Elsevier, Amsterdam; New York).
32. V. M. Janardhanan and O. Deutschmann, "Numerical study of mass and heat transport in solid-oxide fuel cells running on humidified methane." *Chemical Engineering Science*, **62**, 5473 (2007).
33. S. S. Rathore, S. Biswas, D. Fini, A. P. Kulkarni, and S. Giddey, "Direct ammonia solid-oxide fuel cells: A review of progress and prospects." *International Journal of Hydrogen Energy*, **46**, 35365 (2021).

34. L. Wehrle, A. Ashar, O. Deutschmann, and R. J. Braun, "Evaluating high power density, direct-ammonia SOFC stacks for decarbonizing heavy-duty transportation applications." *Applied Energy*, **372**, 123646 (2024).

35. Y. Lin, Z. Zhan, J. Liu, and S. A. Barnett, "Direct operation of solid oxide fuel cells with methane fuel." *Solid State Ionics*, **176**, 1827 (2005).

36. L. Wang et al., "Power-to-methane via co-electrolysis of H_2O and CO_2: The effects of pressurized operation and internal methanation." *Applied Energy*, **250**, 1432 (2019).

37. M. E. Coltrin, R. J. Kee, and F. M. Rupley, "Surface CHEMKIN (Version 4. 0): A Fortran package for analyzing heterogeneous chemical kinetics at a solid-surface—gas-phase interface." *Technical Report*, **SAND-90-8003B**, 6128661 (1991), http://www.osti.gov/servlets/purl/6128661-UX6iLD/.

38. L. Maier, B. Schädel, K. Herrera Delgado, S. Tischer, and O. Deutschmann, "Steam reforming of methane over nickel: development of a multi-step surface reaction mechanism." *Topics in Catalysis*, **54**, 845 (2011).

39. V. M. Janardhanan and O. Deutschmann, "CFD analysis of a solid oxide fuel cell with internal reforming: Coupled interactions of transport, heterogeneous catalysis and electrochemical processes." *Journal of Power Sources*, **162**, 1192 (2006).

40. G. Narasimhaiah and V. M. Janardhanan, "Modeling CO_2 electrolysis in solid oxide electrolysis cell." *Journal of Solid State Electrochemistry*, **17**, 2361 (2013).

41. "Chapter 3: fuel cell reaction kinetics." *Fuel Cell Fundamentals* ch. 3, 77 (John Wiley & Sons, Ltd) (2016).

42. C. H. Wendel, Z. Gao, S. A. Barnett, and R. J. Braun, "Modeling and experimental performance of an intermediate temperature reversible solid oxide cell for high-efficiency, distributed-scale electrical energy storage." *Journal of Power Sources*, **283**, 329 (2015).

43. D. Ferrero, A. Lanzini, P. Leone, and M. Santarelli, "Reversible operation of solid oxide cells under electrolysis and fuel cell modes: Experimental study and model validation." *Chemical Engineering Journal*, **274**, 143 (2015).

44. Y. Wang, A. Banerjee, L. Wehrle, Y. Shi, N. Brandon, and O. Deutschmann, "Performance analysis of a reversible solid oxide cell system based on multi-scale hierarchical solid oxide cell modelling." *Energy Conversion and Management*, **196**, 484 (2019).

45. L. Wehrle, *Multiscale Modeling as a Tool to Optimize the Design and Performance of Solid Oxide Cells for Industrial Applications* (Karlsruher Instituts fuer Technologie (KIT)) (2023), PhD thesis.

46. H. Zhu and R. J. Kee, "Modeling distributed charge-transfer processes in SOFC membrane electrode assemblies." *J. Electrochem. Soc.*, **155**, B715 (2008).

47. A. Bertei and C. Nicolella, "A comparative study and an extended theory of percolation for random packings of rigid spheres." *Powder Technology*, **213**, 100 (2011).

48. A. Bertei and C. Nicolella, "Percolation theory in SOFC composite electrodes: effects of porosity and particle size distribution on effective properties." *Journal of Power Sources*, **196**, 9429 (2011).

49. P. Vijay, M. O. Tadé, Z. Shao, and M. Ni, "Modelling the triple phase boundary length in infiltrated SOFC electrodes." *International Journal of Hydrogen Energy*, **42**, 28836 (2017).

50. J. H. Nam and D. H. Jeon, "A comprehensive micro-scale model for transport and reaction in intermediate temperature solid oxide fuel cells." *Electrochimica Acta*, **51**, 3446 (2006).

51. P.-Y. Lanfrey, Z. Kuzeljevic, and M. Dudukovic, "Tortuosity model for fixed beds randomly packed with identical particles." *Chemical Engineering Science*, **65**, 1891 (2010).

52. R. E. Hayes, *Introduction to Catalytic Combustion* (Routledge, London) (2021).

53. P. Deuflhard, E. Hairer, and J. Zugck, "One-step and extrapolation methods for differential-algebraic systems." *Numerische Mathematik*, **51**, 501 (1987).

54. M. Mortada, H. S. Ramadan, J. Faraj, A. Faraj, H. El Hage, and M. Khaled, "Impacts of reactant flow nonuniformity on fuel cell performance and scaling-up: Comprehensive review, critical analysis and potential recommendations." *International Journal of Hydrogen Energy*, **46**, 32161 (2021).

55. Y. Wang, J. Shi, X. Gu, O. Deutschmann, Y. Shi, and N. Cai, "Toward mobility of solid oxide fuel cells." *Progress in Energy and Combustion Science*, **102**, 101141 (2024).

56. S. Tischer and O. Deutschmann, "Recent advances in numerical modeling of catalytic monolith reactors." *Catal. Today*, **105**, 407 (2005).

57. V. Menon, V. M. Janardhanan, S. Tischer, and O. Deutschmann, "A novel approach to model the transient behavior of solid-oxide fuel cell stacks." *Journal of Power Sources*, **214**, 227 (2012).

58. F. P. Incropera and D. P. DeWitt, *Fundamentals of Heat and Mass Transfer, 4th Edition* 4th ed. (Wiley, New York, NY U.A) (1996).

59. P. Von Böckh and T. Wetzel, *Wärmeübertragung: Grundlagen und Praxis* (Springer, Berlin, Heidelberg) (2014).

60. O. Furst and O. Deutschmann, "Development and calibration of a fast flow model for solid oxide cell stack internal manifolds." *Journal of Power Sources*, **613**, 234857 (2024).

61. S. D. Ebbesen, R. Knibbe, and M. Mogensen, "Co-electrolysis of steam and carbon dioxide in solid oxide cells." *J. Electrochem. Soc.*, **159**, F482 (2012).

62. V. M. Janardhanan and O. Deutschmann, "Modeling diffusion limitation in solid-oxide fuel cells." *Electrochimica Acta*, **56**, 9775 (2011).

63. J. R. Ferguson, J. M. Fiard, and R. Herbin, "Three-dimensional numerical simulation for various geometries of solid oxide fuel cells." *Journal of Power Sources*, **58**, 109 (1996).

64. W. Kiatkittipong, T. Tagawa, S. Goto, S. Assabumrungrat, and P. Praserthdam, "Oxygen transport through LSM/YSZ/LaAlO system for use of fuel cell type reactor." *Chemical Engineering Journal*, **106**, 35 (2005).

65. W. G. Bessler, "Rapid impedance modeling via potential step and current relaxation simulations." *J. Electrochem. Soc.*, **154**, B1186 (2007).

66. A. Nechache, M. Cassir, and A. Ringuedé, "Solid oxide electrolysis cell analysis by means of electrochemical impedance spectroscopy: A review." *Journal of Power Sources*, **258**, 164 (2014).

67. R. Barfod, M. Mogensen, T. Klemenso, A. Hagen, Y.-L. Liu, and P. Vang Hendriksen, "Detailed Characterization of Anode-Supported SOFCs by Impedance Spectroscopy." *J. Electrochem. Soc.*, **154**, B371 (2007).

68. R. Powell, R. Tye, and M. Hickman, "The thermal conductivity of nickel." *International Journal of Heat and Mass Transfer*, **8**, 679 (1965).

69. T. C. Allison, *NIST-JANAF Thermochemical Tables - SRD 13*, **258**, 164 (2013), Accessed 05.06.2024 https://janaf.nist.gov/.

70. M. Radovic, E. Lara-Curzio, R. M. Trejo, H. Wang, and W. D. Porter, "Thermophysical properties of YSZ and Ni-YSZ as a function of temperature and porosity.", ed. N. P. Bansal et al. *Ceramic Engineering and Science Proceedings* 79 (John Wiley & Sons, Inc., Hoboken, NJ, USA) (2008).

71. K. W. Schlichting, N. P. Padture, and P. G. Klemens, *J. Mater. Sci.*, **36**, 3003 (2001).

72. A. Esquirol, N. P. Brandon, J. A. Kilner, and M. Mogensen, "Electrochemical characterization of $La_{0.6}Sr_{0.4}Co_{0.2}O_3$ cathodes for intermediate-temperature SOFCs." *J. Electrochem. Soc.*, **151**, A1847 (2004).

73. Y.-C. Shin, S.-ichi Hashimoto, K. Yashiro, K. Amezawa, and T. Kawada, "Thermal properties of perovskite-type oxides $La_{0.6}Sr_{0.4}Co_1-XFexO_{3-\delta}$ ($0 \leqslant x \leqslant 1.0$)." *ECS Trans.*, **72**, 105 (2016).

74. *VDM Crofer 22 H Data Sheet* (2021), Accessed 04.07.2024 https://www.vdm-metals.com/fileadmin/user_upload/Downloads/Data_Sheets/Data_Sheet_VDM_Crofer_22_H.pdf.

75. *PROMALIGHT: Rigid microporous insulation boards*, Accessed 04.07.2024 https://www.promat.com/en/industry/products-solutions/high-temperatureinsulation/rigid-panels/promalight/.

76. H. Bruus, *Theoretical Microfluidics* (2008), Oxford master series in physics 18 (Oxford University Press) "Oxford; New York."

77. S. Appari, V. M. Janardhanan, S. Jayanti, L. Maier, S. Tischer, and O. Deutschmann, "Micro-kinetic modeling of NH3 decomposition on Ni and its application to solid oxide fuel cells." *Chemical Engineering Science*, **66**, 5184 (2011).